

# PARTICLE ACCELERATION ZONES ABOVE PULSAR POLAR CAPS: ELECTRON AND POSITRON PAIR FORMATION FRONTS

Alice K. Harding & Alexander G. Muslimov<sup>1</sup>

Laboratory for High Energy Astrophysics

NASA/Goddard Space Flight Center

Greenbelt, MD 20771

## ABSTRACT

We investigate self-consistent particle acceleration near a pulsar polar cap (PC) by the electrostatic field due to the effect of inertial frame dragging. Test particles gain energy from the electric field parallel to the open magnetic field lines and lose energy by both curvature radiation (CR) and resonant and non-resonant inverse Compton scattering (ICS) with soft thermal X-rays from the neutron star (NS) surface. Gamma-rays radiated by electrons accelerated from the stellar surface produce pairs in the strong magnetic field, which screen the electric field beyond a pair formation front (PFF). Some of the created positrons can be accelerated back toward the surface and produce  $\gamma$ -rays and pairs that create another PFF above the surface. We find that ICS photons control PFF formation near the surface, but due to the different angles at which the electron and positron scatter the soft photons, positron initiated cascades develop above the surface and screen the accelerating electric field. Stable acceleration from the NS surface is therefore not possible in the presence of dominant ICS energy losses. However, we find that stable acceleration zones may occur at some distance above the surface, where CR dominates the electron and positron energy losses, and there is up-down symmetry between the electron and positron PFFs. We examine the dependence of CR-controlled acceleration zone voltage, width and height above the surface on parameters of the pulsar and its soft X-ray emission. For most pulsars, we find that acceleration will start at a height of 0.5 - 1 stellar radii above the NS surface.

*Subject headings:* pulsars: electrodynamics — pulsars: high-energy emission  
— pulsars: pair production — pulsars: particle acceleration — stars:  
neutron

## 1. INTRODUCTION

The theory of particle acceleration in pulsar magnetospheres has been under development for almost three decades. Although it was well known that rotating magnetic dipoles would induce

---

<sup>1</sup>NAS/NRC Senior Research Associate

electric fields in vacuum (Deutsch 1955), it took several years after the discovery of pulsars to realize that the huge vacuum fields could not in practice be available for particle acceleration. The electric field parallel to the magnetic field is at least partly screened by particles supplied from the stellar surface (Goldreich & Julian 1969) or by electron-positron avalanches (Sturrock 1971). The true accelerating voltage of a pulsar must be determined by departures from the corotation, or Goldreich-Julian charge density, that could completely screen the parallel electric field. Several types of models have studied pulsar acceleration due to charge deficits at different locations in the magnetosphere. Polar cap (PC) models consider the formation of a parallel electric field in the open field region near the magnetic poles, while outer gap models consider acceleration in the outer magnetosphere, near the null charge surface (see Mestel 1998 for the most recent and comprehensive review of pulsar electrodynamics). Ruderman & Sutherland (1975; hereafter RS75) introduced a PC model invoking a vacuum gap due to the trapping of ions in the neutron star (NS) crust. The calculations by Jones (1985, 1986), and Neuhauser et al. (1986, 1987) seem to favor a low value for the work function (at least a factor of 10 less than it was thought earlier) in the NS surface with a strong magnetic field. The important implication of this study is that the possibility of free ejection of charges (actually of both signs) from the NS surface can be now, at least theoretically, justified. In this paper, we concentrate on a space-charge limited flow model (implying very low work function in the NS surface) based originally on the work of Arons & Scharlemann (1979; hereafter AS79), who determined the electric field produced by the small departure from the Goldreich-Julian charge that grows above the surface due to the geometry of the open dipole field. The electric field accelerating electrons in this model developed along only field lines that curved toward the rotation axis (“favorably” curved field lines), so that acceleration occurred over half of the PC. The parallel field is shorted-out at a height above the surface where the  $\gamma$ -rays from accelerated particles produce sufficient electron-positron pairs in the strong magnetic field. The accelerating potential is thus limited by such a pair formation front (PFF).

These initial calculations of electron-positron PFFs assumed that the primary electrons began accelerating at the NS surface and that curvature radiation (CR) was the only mechanism for providing pair-producing photons (Arons 1983; hereafter A83). In recent years, it has become clear that inverse-Compton scattering (ICS) of soft thermal X-ray photons from the hot NS surface by the primary electrons is also an important mechanism above the PC. As well as being a significant energy loss (Kardashëv et al. 1984, Xia et al. 1985, Daugherty & Harding 1989, Sturmer 1995; hereafter S95) and radiation (Sturmer & Dermer 1994) mechanism, ICS can also provide photons capable of producing pairs. Pulsed X-rays have been detected from a number of pulsars which are consistent with blackbody spectra at temperatures around  $10^5 - 10^6$  K (Ogelman 1995). Zhang & Qiao (1996) and Zhang et al. (1997; hereafter ZQLH97) first explored the effect of the pairs from inverse-Compton photons on the acceleration in a Ruderman-Sutherland type model. They found that ICS photons may produce a PFF sooner (at a lower altitude) than the CR photons would from the same accelerating electrons. In fact in this case, the electrons will stop accelerating before they can emit significant CR. The standard models of PC acceleration thus need substantial revision.

Another effect which has never been included in PC acceleration models is the formation of a lower PFF due to the positrons that are turned around and accelerated downward from the electron PFF. Although the number of positrons which are accelerated downward is small compared to the number of primary electrons and even to the charge deficit near the upper PFF, the multiplicity of the downward cascades is quite large (as we will discuss in Section 3.1). Thus, the amount of charge produced by only a small number of downward moving positrons may be sufficient to establish a second PFF. Although downward going cascades have been discussed in previous papers (see e.g. AS79), their effect on the acceleration of primaries has not been investigated. Daugherty & Harding (1996, hereafter DH96) qualitatively discussed the effects of pair cascades by returning positrons, their creation of pairs within the acceleration zone and the need for a self-consistent model of PC acceleration.

In this paper, we present a detailed study of the acceleration of primary electrons and secondary (downward-moving) positrons above a pulsar PC, assuming space-charge limited flow (free emission) of particles from the NS surface (see Harding & Muslimov 1998, for a review). We include the general relativistic effect of inertial frame-dragging, which induces a much larger electric field than that expected in the flat spacetime and is not limited to favorably-curved field lines (Section 2.1). This is important because, as has been concluded earlier in papers by Fawley, Arons & Scharlemann (1977) and A83, the potential drops (derived for flat space-time) are not sufficient to account for observed pulsar  $\gamma$ -rays. Both electrons and positrons suffer energy loss and emit photons from CR and ICS. The treatment of ICS of both upward and downward moving particles requires revisions from previous studies of only upward moving particles (Dermer 1990; hereafter D90; S95), which are presented in Section 2.2.2. We then compute the location of both electron and positron PFFs due to one-photon pair production as a function of magnetic colatitude and height of the lower PFF. We also discuss in Section 2.4 the fraction of positrons that are turned around at the upper PFF. When the electrons are assumed to accelerate from the NS surface, we find that ICS photons produce the PFFs (Section 3.1), in agreement with the results of ZQLH97. However, we also find that there is substantial difference between the scattering of upward-going electrons and downward-going positrons by the same thermal X-ray photons: the electrons scatter these photons at angles less than  $\pi/2$ , while the positrons scatter the photons head-on. Electrons produce pairs through resonant scattering, while positrons produce pairs by scattering above the cyclotron resonance. The photons scattered by positrons are therefore more energetic and produce pairs in a shorter distance. These pairs may screen the accelerating field up to some distance above the surface. We find that stable, double PFFs can form only when CR photons produce them, i.e. at a height where CR losses overtake ICS losses. We compute the height of these stable PFFs as a function of pulsar period and surface field strength (Section 3.1). One interesting result is that the acceleration voltage limited by CR-controlled PFFs is only a function of magnetic colatitude (i.e. geometry of the open field lines), ranging between  $\sim 10^7$  and  $3 \times 10^7 mc^2$ , and is insensitive to pulsar parameters such as period and surface value of the magnetic field strength and even to the height of the acceleration. The stable location of the lower PFF depends primarily on surface magnetic field, temperature and size of the hot polar

cap, ranging between 0.5 and 1.0 stellar radius, but is insensitive to period. Implications of these results for high-energy pulsar emission are discussed in Section 4.

## 2. CALCULATION OF PAIR FORMATION FRONTS

We consider a test particle approach to the determination of PFF locations. The test particles in this case are electrons or positrons that gain energy through electrostatic acceleration and lose energy through radiative losses. Photons are created by CR and ICS and destroyed by magnetic pair creation. We assume that the electric field is completely screened at the point where the first pair is produced. This is a good assumption for several reasons. First, as discussed in more detail below, the electric field arises due to a small imbalance between the actual charge density and the local, rotation-induced, Goldreich-Julian charge density. It therefore does not require much additional charge to short-out this field. Second, the onset of pair cascading occurs very quickly (DH96), so that the number of pairs produced per primary particle increases rapidly over small distances. Thus, as found in A83, the width of the PFF (the screening distance of the electric field) is very small compared to other dimensions of the problem. Figure 1 illustrates the geometry of the calculation. Suppose that the PFF results from pairs produced by  $\gamma$ -rays of energy  $\varepsilon_{\min}$  (in units of  $mc^2$ ) radiated by particles of energy  $\gamma_{\min}$ . The distance of the PFF from the starting point of the particle acceleration at  $h_0$  is then:

$$S_c = \min[S_a(\gamma_{\min}) + S_p(\varepsilon_{\min})] \quad (1)$$

where  $S_a(\gamma_{\min})$  is the distance required to accelerate the particle until it can radiate a photon of energy  $\varepsilon_{\min}$ , and  $S_p(\varepsilon_{\min})$  is the pair attenuation length of the photon. The acceleration distance,  $S_a(\gamma_{\min})$ , is determined by first integrating the equation of motion of the particle to determine its energy as a function of its pathlength  $s$ :

$$c \frac{d\gamma}{ds} = \frac{e}{mc} E_{\parallel} - \dot{\gamma}_{\text{IC}} - \dot{\gamma}_{\text{CR}}, \quad (2)$$

where  $E_{\parallel}$  is the electric field induced parallel to the magnetic field,  $\dot{\gamma}_{\text{IC}}$  and  $\dot{\gamma}_{\text{CR}}$  are the loss rates for ICS and CR. Discussion of these processes will be given in Sections 2.1 and 2.2. The pair production attenuation length of photons radiated by the particle through either ICS or CR is then determined. This attenuation length  $S_p(\varepsilon)$ , defined to be the path length over which the optical depth is unity, is given by

$$\tau(\varepsilon) = \int_0^{S_p(\varepsilon)} T_{\text{pp}}(\theta_{\text{kB}}, \varepsilon) ds = 1 \quad , \quad (3)$$

where  $ds$  is the pathlength differential along the photon momentum vector  $\mathbf{k}$ ,  $T_{\text{pp}}$  is the attenuation coefficient for one-photon pair production and  $\theta_{\text{kB}}$  is the angle between  $\mathbf{k}$  and the local magnetic field direction. Computation of  $S_p(\varepsilon)$  will be discussed in Section 2.3. As we will discuss in Section 3.1, when ICS causes the PFF<sup>+</sup> and PFF<sup>-</sup>,  $S_c^+$  is smaller than  $S_c^-$ , due to different modes of ICS. The PFF<sup>+</sup> will then not coincide with the start of the electron acceleration at  $h_0$ .

## 2.1. Polar Cap Electrodynamics

We use the electric field due to inertial frame dragging above the NS surface, first calculated by Muslimov & Tsygan (1990, 1992; hereafter MT90, 92). The regime under which the generation of this field occurs is actually the same as implied in the electric field computations in flat spacetime by AS79, that of space-charge limited flow. An electric field must be present above the NS surface because as charges flow along open magnetic field lines, the corotation, or Goldreich-Julian charge density  $\rho_{\text{GJ}}$ , cannot be maintained. Even though  $\rho = \rho_{\text{GJ}}$  and therefore  $E_{\parallel} = 0$  at the surface, the curvature of the field lines causes the area of the open field region, through which the particles flow, to increase faster than  $\rho_{\text{GJ}}$ , and a charge deficit grows with distance. Thus, the  $E_{\parallel}$  grows with height up to about one stellar radius above the surface, and then drops off. It is important that for a nearly aligned NS in flat spacetime, the space-charge density of the outflowing particles (electrons) proved to be almost exactly compensated by the effective Goldreich-Julian charge density, thus resulting in the substantial suppression of the electric field in the region of open field lines. General relativity causes a significant modification of the mechanism of the electric field induction, through the effect of dragging of inertial frames, a consequence of the distortion of spacetime by a rotating gravitating body. An observer near a rotating mass experiences a force and must corotate to remain in an inertial frame, with an angular velocity that decreases with distance from the rotating mass. The charge density above a NS surface must be computed in a local inertial frame that is rotating with respect both to the NS and to an observer at infinity. Thus the Goldreich-Julian charge density, which is the charge density required to make magnetospheric particles drift in corotation with the star, will differ from that in flat spacetime. This charge difference enhances  $E_{\parallel}$  over what it would be in flat spacetime, by a factor of 50 - 100 for a typical 1 s pulsar. The frame-dragging contribution to  $E_{\parallel}$  that signifies the striking difference between the general relativistic and classical treatments of NS electrodynamics is proportional to  $\cos \chi$  (see equation [18] below), where  $\chi$  is the angle between the magnetic and spin axes of the pulsar. [Obviously, there is also a frame-dragging contribution to  $E_{\parallel}$  which is proportional to  $\sin \chi$ , but it is comparable to that produced in a flat spacetime limit.] Particle acceleration may therefore occur throughout the entire open field line region, with the relative contribution of the frame dragging component to  $E_{\parallel}$  being strongest for pulsars with small obliquities.

Muslimov & Harding (1997; hereafter MH97) derived expressions for the  $E_{\parallel}$  due to frame dragging in two limits: close enough to the NS surface such that  $z = s/R \ll \theta_0$ , where  $\theta_0$  is the PC half-angle, and far from the surface such that  $z \gg \theta_0$ . These expressions were derived from solutions to Poisson's equations assuming boundary conditions  $E_{\parallel} = 0$ , as well as the potential  $\Phi = 0$  at the stellar surface and along the last open field line. We have adapted these solutions for use in this paper by incorporating the screening effect of an upper boundary at  $z_c = S_c/R$ , i.e. of the pair formation front, where  $E_{\parallel}(z = z_c) = 0$ . Although this approach is not fully self-consistent, in Section 2.1.1 we discuss how the screening of the electric field at the upper boundary could be included in our calculations in a self-consistent way. In this paper we also explore the situation where the positrons flowing back to the PC surface initiate electron-positron cascades. Although

this possibility has been discussed since the very first papers on pulsar electrodynamics (see e.g. AS79), it has never been addressed at an appropriate quantitative level. Here we attempt to approach this and some other related problems from the quantitative point of view which, we believe, can advance our understanding of the PC electrodynamics and its relevance to the modeling of  $\gamma$ -ray emission from pulsars.

We note that the derivation of formulae for the electric field (potential) we exploit in the present analysis implies that the angle  $\theta_0$  (magnetic colatitude of the polar field line) is small, which is a very good approximation for the region of open magnetic field lines in most pulsars. However, it is instructive to look at the general-relativistic expression for the Goldreich-Julian charge density that contains a contribution of order of  $\theta^2$  to the main term. This expression reads

$$\rho_{\text{GJ}} = -\frac{\Omega B_0}{2\pi c\alpha\eta^3} \frac{f(\eta)}{f(1)} \left\{ \left[ \left(1 - \frac{\kappa}{\eta^3}\right) - \frac{3}{2}H(\eta)\theta^2 \right] \cos\chi + \frac{3}{2}H(\eta)\theta \sin\chi \cos\phi \right\}, \quad (4)$$

where  $\Omega$  is the NS rotation frequency,  $B_0$  is the surface value of the magnetic field strength at the magnetic pole,  $\alpha = (1 - \epsilon/\eta)^{1/2}$  is the red-shift function,  $\epsilon = r_g/R$ ,  $r_g$  is the gravitational radius of the NS,  $R$  is the stellar radius,  $\eta = r/R$  is the dimensionless radial coordinate,  $\kappa = \epsilon I/MR^2$ ,  $I$  and  $M$  are the moment of inertia and mass of the NS, respectively, and the functions  $f(\eta)$  and  $H(\eta)$  are defined below (see equations [8], [16]). In formula (4) the functions  $f$  and  $H$  should be evaluated at  $\eta = r/R$  and  $\epsilon = r_g/R$ . In our derivation of the general-relativistic electrodynamic equations we neglect the contribution to the electric field produced by the flaring of the magnetic field lines, which is a factor of  $\sim \theta^{-2} \sim 500$  ( $P/0.1$  s) (where  $P$  is the pulsar spin period) smaller than that produced by the frame dragging. This contribution results from the second-order terms like that in the square bracket of equation [4]. [In Section 2.4 we will refer to this equation to clarify yet another important issue.] The small-angle approximation may not be accurate enough for the millisecond pulsars, for which  $\theta \sim 0.3$  ( $r/R$ ) $^{1/2}$ ( $P/2$  ms) $^{-1/2}$ . We also note that the effect of the electric field generation by the frame dragging does not depend on the particular configuration of the stellar magnetic field, simply because while the distribution of the real space charge in the acceleration region is mainly determined by the flaring of the magnetic field lines, the effect of frame dragging on the Goldreich-Julian charge density is independent of the geometry of the polar field lines. This means that one cannot mimic the frame dragging effect simply by distorting the polar magnetic flux tube.

### 2.1.1. Rescaling of $E_{\parallel}$ with no upper PFF

The possibility of electron-positron cascades near the stellar surface initiated by the backflowing positrons unavoidably implies that the bottom of the polar magnetic flux tube should be treated as a highly-conducting layer of an electron-positron plasma on the top of the PC surface, rather than as a regular NS surface made of iron or hydrogen atoms in the strong magnetic field. In a more extreme case (see e.g. Wang et al. 1998), which seems to be less justified at the moment, the whole NS surface may be covered by a thin electron-positron plasma layer.

Note that the presence of such a layer even on the top of the PC should substantially affect the electrodynamics and therefore the acceleration of charged particles in the region of open magnetic field lines. It will allow the free supply of charges into the acceleration region, a requirement for space-charge limited flow. Also, we shall discuss in Section 3, a self-consistent regime with double PFFs that may significantly differ from the standard one implying a single PFF above the stellar surface.

In this Section and the next, we discuss the principal modifications one must introduce into the treatment of the acceleration region to incorporate the effects resulting from the occurrence of double PFFs. First of all, the appropriate distance variables in  $E_{\parallel}$  should be rescaled by an “effective” NS radius  $R_E = R + h_0$  (cf. Fig 1), which is now assumed to be the lower boundary of the acceleration, such that  $E_{\parallel}(z = 0) = 0$ , where  $z \equiv s/R_E$  is the dimensionless altitude above the effective surface. The expressions for the electric field are thus symmetric between the lower and upper boundaries, in the sense that they allow the proper treatment of e.g. both primary electron and secondary positron acceleration, which is an essential requirement for the theory.

To clarify our analytic solutions (see Section 2.1.2) for the rescaled electric potential (accelerating electric field) produced between the lower and upper pair fronts, let us consider the expression for the electric potential in terms of the difference between the actual and Goldreich-Julian charge densities  $\rho - \rho_{\text{GJ}}$ . Because  $\rho$  and  $\rho_{\text{GJ}}$  are just linear combinations of  $\sin \chi$  and  $\cos \chi$ , we can write the potential  $\Phi$  in the simple form (at distances from the stellar surface greater than the PC size) as

$$\Phi = \alpha S(r) \left[ (\rho - \rho_{\text{GJ}})|_{\chi=0} \cos \chi + \frac{1}{2} (\rho - \rho_{\text{GJ}})|_{\chi=\frac{\pi}{2}} \sin \chi \right] (1 - \xi^2), \quad (5)$$

where  $S(r) \equiv \pi[r\theta(\eta)]^2$  is the cross-sectional area of the polar magnetic flux tube at the radial distance  $r$  and  $(\rho - \rho_{\text{GJ}})|_{\chi=0}$  and  $(\rho - \rho_{\text{GJ}})|_{\chi=\frac{\pi}{2}}$  are the coefficients of  $\cos \chi$  and  $\sin \chi$  in the expression for  $(\rho - \rho_{\text{GJ}})$  (see equations [10] and [11]). It also says that the local value of the electric potential is of order of the local value of the effective space charge (equal to the difference between the real space charge and induced Goldreich-Julian space charge) divided by the characteristic longitudinal length scale. The expression (5) does not incorporate the effect of the screening of the electric field at the upper boundary (PFF). This effect is included in the corresponding expressions we discuss later in Section 2.1.2. The relation (5) gives the correct solution for the electric potential and longitudinal component of the electric field for altitudes greater than the PC size and satisfying the  $\Phi = 0$  and  $E_{\parallel} = 0$  boundary conditions at the (effective) stellar surface, where  $\rho = \rho_{\text{GJ}}$ . This expression is very useful for illustrating the modification of the potential and longitudinal component of the electric field resulted from the redefining of the position of the lower zero-electric field boundary (set e.g. by the lower PFF produced by the backflowing positrons). It explains the physical meaning of such a modification, which is simply a readjustment of the true charge outflow (in the regime of self-limitation) to the local value of the Goldreich-Julian charge density at the effective surface, and allows us to better understand the corresponding exact analytic solution.

We introduce the radial coordinate scaled by effective radius  $R_E$ ,  $\eta \equiv 1 + z = (R_E + s)/R_E$ , and transverse coordinate  $\xi \equiv \theta/\theta(\eta)$ , the magnetic colatitude scaled by the half-opening angle of the polar magnetic flux tube,

$$\theta(\eta) = \theta_0 \left[ \eta \frac{f(1)}{f(\eta)} \right]^{1/2} \quad (6)$$

at radius  $\eta$ , where

$$\theta_0 = \left[ \frac{\Omega R_E}{c f(1)} \right]^{1/2} \quad (7)$$

is the PC half-angle at the effective surface  $R_E$ , and

$$f(\eta) = -3 \left( \frac{\eta}{\epsilon} \right)^3 \left[ \ln \left( 1 - \frac{\epsilon}{\eta} \right) + \frac{\epsilon}{\eta} \left( 1 + \frac{\epsilon}{2\eta} \right) \right] \quad (8)$$

is the correction factor for the dipole component of the magnetic flux through the magnetic hemisphere of radius  $r$  in a Schwarzschild metric (MH97).

Note that in equation (5)

$$S(r) \equiv \pi \frac{\Omega}{c} \frac{r^3}{f(\eta)}. \quad (9)$$

The expressions for  $\rho$  and  $\rho_{GJ}$ , valid for any radius, can be written as (see e.g. MH97)

$$\rho = -\sigma(r) \left[ (1 - \eta_*^2 \kappa) \cos \chi + \frac{3}{2} \theta_0 H(1) \xi \sin \chi \cos \phi \right], \quad (10)$$

$$\rho_{GJ} = -\sigma(r) \left[ (1 - \eta_*^2 \frac{\kappa}{\eta^3}) \cos \chi + \frac{3}{2} \theta(\eta) H(\eta) \xi \sin \chi \cos \phi \right]. \quad (11)$$

In these expressions

$$\sigma(r) \equiv \frac{1}{2} \left( \frac{\Omega}{c} \right)^2 R^3 \frac{B_0}{f(\eta_*)} \frac{1}{\alpha S(r)}, \quad (12)$$

where  $\eta_* = R/R_E$  ( $0.5 \lesssim \eta_* \lesssim 1$ , as it will be shown below).

Thus, after substituting the above expressions for  $\rho$  and  $\rho_{GJ}$  into equation (5) we get the following formulae for the rescaled electric potential

$$\begin{aligned} \Phi = & \frac{1}{2} \Phi_0 \theta_0^2 \eta_*^2 \left\{ \eta_*^2 \kappa \left( 1 - \frac{1}{\eta^3} \right) \cos \chi + \right. \\ & \left. \frac{3}{4} [\theta(\eta) H(\eta) - \theta_0 H(1)] \xi \sin \chi \cos \phi \right\} (1 - \xi^2), \end{aligned} \quad (13)$$

and the accelerating component of the electric field

$$E_{\parallel} = -E_0 \theta_0^2 \eta_*^2 \left[ \frac{3}{2} \eta_*^2 \frac{\kappa}{\eta^4} \cos \chi + \frac{3}{8} \theta(\eta) H(\eta) \delta(\eta) \xi \sin \chi \cos \phi \right] (1 - \xi^2), \quad (14)$$

where  $\Phi_0 \equiv B_0(\Omega R/c) R f(1)/f(\eta_*)$ , and  $E_0 \equiv \Phi_0/R$ . The quantities  $\epsilon$  and  $\kappa$  in all expressions derived in this Section for the rescaled radial coordinate now read

$$\epsilon \equiv \frac{2GM}{R_E c^2}, \quad \kappa \equiv \frac{\epsilon I}{MR^2}. \quad (15)$$



Finally, the functions

$$H(\eta) = \frac{\epsilon}{\eta} - \frac{\kappa}{\eta^3} + \left(1 - \frac{3\epsilon}{2\eta} + \frac{\kappa}{2\eta^3}\right) \left[f(\eta) \left(1 - \frac{\epsilon}{\eta}\right)\right]^{-1}, \quad (16)$$

$$\delta(\eta) = \frac{\partial}{\partial \eta} \ln [H(\eta)\theta(\eta)] \quad (17)$$

are both evaluated at  $\eta = r/R_E$ .

### 2.1.2. Screened $E_{\parallel}$ with upper PFF

We now include the effect of the electric field screening at the upper PFF, at  $\eta = \eta_c = (R + h_c)/R_E$ , by obtaining the solution to Poisson's equation with the upper boundary condition,  $E_{\parallel}(\eta = \eta_c) = 0$ . In the limit where  $z_c \ll 1$  and  $z \leq z_c$  the accelerating component of the electric field reads

$$E_{\parallel} \simeq -E_0 \theta_0^3 (1 - \epsilon)^{1/2} \eta_*^2 \left\{ \eta_*^2 \left[ \sum_{i=1}^{\infty} A_i J_0(k_i \xi) \right] \cos \chi + \left[ \sum_{i=1}^{\infty} B_i J_1(\tilde{k}_i \xi) \right] \sin \chi \cos \phi \right\}, \quad (18)$$

where,

$$A_i = \frac{3}{2} \kappa \left[ \frac{8}{k_i^4 J_1(k_i)} \right] \mathcal{F}_i(z, \gamma_i), \quad B_i = \frac{3}{8} \theta_0 H(1) \delta(1) \left[ \frac{16}{\tilde{k}_i^4 J_2(\tilde{k}_i)} \right] \mathcal{F}_i(z, \tilde{\gamma}_i), \quad (19)$$

$$\mathcal{F}(z, \gamma) = -[a_1(\gamma\eta - 1)e^{\gamma z} + a_2(\gamma\eta + 1)e^{-\gamma z} + a_1(1 - \gamma) - a_2(1 + \gamma)] / (a_1 + a_2), \quad (20)$$

$$a_1 = (\gamma\eta_c + 1)e^{-\gamma z_c} - \gamma - 1, \quad a_2 = \gamma - 1 - (\gamma\eta_c - 1)e^{\gamma z_c}, \quad (21)$$

and

$$\gamma_i \approx \frac{k_i}{\theta_0(1 - \epsilon)^{1/2}}, \quad \text{and} \quad \tilde{\gamma}_i \approx \frac{\tilde{k}_i}{\theta_0(1 - \epsilon)^{1/2}}, \quad (22)$$

where  $k_i$  and  $\tilde{k}_i$  are the positive roots of the Bessel functions  $J_0$  and  $J_1$ , respectively. In expressions (20), (21)  $\gamma = \gamma_i$  or  $\tilde{\gamma}_i$  should be used. In the limit, where  $z \equiv \eta - 1 \gg \theta_0$  and  $z_c \equiv \eta_c - 1 \gg \theta_0$  (cf. Appendix A, equation [A4]),

$$E_{\parallel} \simeq -E_0 \theta_0^2 \eta_*^2 \left\{ \frac{3}{2} \frac{\kappa}{\eta^4} \eta_*^2 \left[ (1 - \xi^2) - \left(\frac{\eta}{\eta_c}\right)^3 \sum_{i=1}^{\infty} \frac{8J_0(k_i \xi)}{k_i^3 J_1(k_i)} e^{-\gamma_i(\eta_c)(\eta_c - \eta)} \right] \cos \chi + \frac{3}{8} \delta(\eta) H(\eta) \theta(\eta) \left[ \xi(1 - \xi^2) - \frac{\eta_c \theta(\eta_c) \delta(\eta_c) H(\eta_c)}{\eta \theta(\eta) \delta(\eta) H(\eta)} \sum_{i=1}^{\infty} \frac{16J_1(\tilde{k}_i \xi)}{\tilde{k}_i^3 J_2(\tilde{k}_i)} e^{-\tilde{\gamma}_i(\eta_c)(\eta_c - \eta)} \right] \sin \chi \cos \phi \right\} \quad (23)$$

where now,

$$\gamma_i = \frac{k_i}{\theta(\eta_c)\eta_c(1 - \epsilon/\eta_c)^{1/2}}, \quad \text{and} \quad \tilde{\gamma}_i = \frac{\tilde{k}_i}{\theta(\eta_c)\eta_c(1 - \epsilon/\eta_c)^{1/2}} \quad (24)$$

Simple analytic expressions can be derived in several limiting cases some of which are summarized in Appendix A (for the radial coordinate scaled by the true stellar radius). The solutions (18) and (23) thus incorporate both the effect of the rescaled lower boundary and screening of the electric field at the upper boundary, and we will use them in our numerical calculations described later on in Section (3.1).

## 2.2. Radiation Production and Losses

In this section, we describe our treatment of the radiation processes that affect the polar cap particle acceleration. This includes energy losses due to CR and ICS, and pair production by the photons from these processes. Although the particles are radiating a full spectrum of photons, we are concerned here only with the pair producing photons. In the interest of making our numerical code as efficient as possible (but with some loss of accuracy), we do not model the entire radiation spectrum of each process, but compute pair production attenuation lengths for a single representative photon energy at each step along the particle path.

### 2.2.1. Curvature radiation

The CR loss rate for particles of charge  $e$  moving along a magnetic field with radius of curvature  $\rho_c$  is

$$-\dot{\gamma}_{\text{CR}} = \frac{3e^2}{2mc^2} \frac{c}{\rho_c^2} \gamma^4. \quad (25)$$

The radius of curvature of the magnetic field in a Schwarzschild metric is

$$\rho_c \simeq \frac{4}{3} \left( \frac{c}{\Omega r} \right)^{1/2} r G(x), \quad \text{and} \quad G(x) = \frac{(1-x)^{3/2} f^{5/2}(x)}{9 - 2f(x)(4 - 3x)} \quad (26)$$

in the small angle limit, where  $x = r_g/r$ ,  $r_g = 2GM/c^2$  is the gravitational radius, and the function  $f(x)$  has been defined in equation (8). Formula (26) gives a slightly larger radius of curvature than the flat-space formula does (by a factor of  $G$ , about 25 – 30%, for the NS parameters we assume in this paper). This can be easily understood, since the strong gravity of the NS tends to increase the flaring of the polar field lines, and therefore the last open field lines (i.e. those reaching the light cylinder at their “turning-points”) should emanate from slightly smaller magnetic colatitudes. In other words, the polar field lines get slightly straighten out, and the effective PC radius slightly decreases (by the same  $\sim 25 - 30\%$ , see also Gonthier & Harding 1994).

The spectrum of CR photons from a particle with energy  $\gamma$  is a power law at low frequencies, with an exponential decline at high frequencies:

$$n_{\text{CR}}(\varepsilon) \propto \begin{cases} \varepsilon^{1/3}, & \varepsilon \ll \varepsilon_{\text{cr}} \\ \exp(-\varepsilon/\varepsilon_{\text{cr}}), & \varepsilon > \varepsilon_{\text{cr}} \end{cases} \quad (27)$$

where  $\varepsilon_{\text{cr}} = (3/2)(\hbar/mc)\gamma^3/\rho_c$  is the critical frequency. Since the one-photon pair attenuation coefficient (equation [48]) increases sharply with energy as  $\exp(-8/3\varepsilon B' \sin \theta_{\text{kB}})$ , the photons from the exponential tail of the curvature spectrum will produce the bulk of the pairs. Here, and in subsequent Sections, the local dipole magnetic field strength is

$$B' = \left(\frac{B_0}{B_{\text{cr}}}\right) \left(\frac{R}{R_E}\right)^3 \left[\frac{f(1)}{f(\eta_*)}\right]. \quad (28)$$

where  $B_{\text{cr}} = 4.413 \times 10^{13}$  G is the critical field strength. The overlap of the curvature spectrum and the pair attenuation coefficient will fall in a narrow frequency band, which we can approximate in a steepest descents analysis as a Gaussian of width,  $\Delta\varepsilon_p = (3B'\varepsilon_p^3 \sin \theta_{\text{kB}})^{1/2}$ , with a mean energy  $\varepsilon_p = (8\varepsilon_{\text{cr}}/3B' \sin \theta_{\text{kB}})^{1/2}$ . Photons will pair produce roughly when  $\varepsilon_p B' \sin \theta_{\text{kB}} \sim 0.2$  for  $B' < 0.1$  and as soon as threshold  $\varepsilon_p \sin \theta_{\text{kB}} = 2$ , is reached, for  $B' > 0.1$  (Daugherty & Harding 1983; hereafter DH83). We therefore have

$$\begin{aligned} \varepsilon_p &= 13.3 \varepsilon_{\text{cr}}, & \Delta\varepsilon_p &= 0.273 \varepsilon_p, & B' &< 0.1 \\ \varepsilon_p &= 4 \varepsilon_{\text{cr}}/3B', & \Delta\varepsilon_p &= 0.87B'^{1/2} \varepsilon_p, & B' &> 0.1 \end{aligned} \quad (29)$$

At each step along the particle acceleration path, pair attenuation lengths are computed for up to five CR photons with energies evenly distributed between  $\varepsilon_p$  and  $\varepsilon_p + 4\Delta\varepsilon_p$ . The first finite value (if any) of the pair attenuation length is taken as  $S_p$  for that step.

### 2.2.2. Inverse Compton scattering

As the particles are accelerated, they may scatter soft photons from the hot NS surface. Due to the strong magnetic field, the ICS cross section is resonant at frequencies where electrons may be excited to higher Landau states and is strongly suppressed (for extraordinary mode photons) below the fundamental. Although the full QED scattering cross section for this process has been calculated (e.g. Daugherty & Harding 1986, Bussard et al. 1986), it is quite unwieldy for numerical calculations. However, the magnetic scattering cross section in the Thomson limit (Canuto et al. 1971) is much simpler and has been used in place of the full QED cross section in almost all astrophysical applications. It includes only the resonance at the cyclotron fundamental (i.e. scattering in the ground state with no excitation) and approaches the Thomson cross section at frequencies above the cyclotron energy.

In this paper, we follow the treatment of S95, who derived simple expressions for electron energy loss rates for magnetic Compton scattering in the Thomson limit, expanding the treatment

of D90 to include the Klein-Nishina suppression above the resonance. Dermer’s approach was to divide the Compton scattering loss rates into three components, each due to the different behavior of the cross section in the regions below the resonance (which he called “angular” scattering due to the strong angle dependence), in the resonance (“resonant” scattering) and above the resonance (“non-resonant” scattering). He assumed that the resonant part of the cross section was a  $\delta$ -function at the cyclotron energy, and that the soft photon source was a blackbody of temperature  $T_b$  radiated by a hot PC of radius  $R_T$ . He derived the scattering loss rates for electrons moving away from the NS surface, so that the soft photon density decreases with height, due to a dilution factor. We have expanded this treatment by computing the associated loss rates for particles (in our case, positrons, although the sign of charge makes no difference for Compton scattering) moving toward the NS surface. In this case, the particles approach the soft photons “head-on”, scattering them to higher energies than the downward moving particles.

The Compton scattering energy loss rate for a particle of energy  $\gamma$  moving through a photon field,  $n_{\text{ph}}(\varepsilon)$ , that is uniform between angles  $\mu_- < \mu < \mu_+$ , from equation (12) of D90, is

$$-\dot{\gamma}_{\text{IC}} = \frac{c}{\mu_+ - \mu_-} \int_0^{[\gamma(1-\beta\mu_-)]^{-1}} d\varepsilon n_{\text{ph}}(\varepsilon) \int_{\mu_-}^{\mu_+} d\mu (1-\beta\mu) \int_{-1}^1 d\mu'_s \int_0^{\varepsilon'_{s,max}} d\varepsilon'_s \left( \frac{d\sigma'}{d\mu'_s d\varepsilon'_s} \right) (\varepsilon_s - \varepsilon), \quad (30)$$

where  $\varepsilon'_{s,max} = \gamma\varepsilon(1 - \beta\mu)$  is the maximum scattered energy in the particle rest frame. Here, primes are used to denote quantities in the particle rest frame and the subscript  $s$  denotes scattered quantities. Thus,  $\sigma'$  is the rest frame scattering cross section. Based on these expressions, the loss rates for the three parts of the cross section,  $\dot{\gamma}_{\text{IC}} = \dot{\gamma}_{\text{ang}} + \dot{\gamma}_{\text{res}} + \dot{\gamma}_{\text{KN}}$ , used in equation (30) can be written

$$-\dot{\gamma}_{\text{ang}} = 46.1 T_6^4 (1 - \mu_c) f_{\text{ang}} \text{ s}^{-1}, \quad (31)$$

$$-\dot{\gamma}_{\text{res}} = 4.9 \times 10^{11} \left[ \frac{T_6 B_{12}^2}{\beta\gamma} \right] f_{\text{res}} \text{ s}^{-1}, \quad (32)$$

$$-\dot{\gamma}_{\text{KN}} = 3.7 \times 10^{11} \left( \frac{T_6}{\beta\gamma^2} \right) \int_{\varepsilon'_-}^{\varepsilon'_+} d\varepsilon' [\varepsilon_0 + \varepsilon_0/\varepsilon' - \gamma] f_{\text{KN}} \text{ s}^{-1}, \quad (33)$$

where  $T_6 \equiv T_b/10^6$  K is the NS surface temperature,  $B_{12}$  is the local dipole magnetic field strength in units of  $10^{12}$  G. equation (33) assumes a  $\delta$ -function at energy  $\varepsilon_0 = 2.7\theta_T$ , where  $\theta_T = kT/mc^2$ , for the distribution of soft thermal photons, and

$$f_{\text{ang}} = \frac{\gamma^2 - 2}{\gamma^2 - 1} - \frac{(\mu_+^3 - \mu_-^3)}{3(\mu_+ - \mu_-)} - \frac{(\mu_+ + \mu_-)}{2\beta\gamma^2} + \frac{\ln[(1 - \beta\mu_-)/(1 - \beta\mu_+)]}{\beta^3\gamma^4(\mu_+ - \mu_-)}, \quad (34)$$

$$f_{\text{res}} = \left( 1 - \frac{\varepsilon_B}{3} \right) \ln \left[ \frac{1 - e^{-w_+}}{1 - e^{-w_-}} \right] + \left( \frac{2}{3} - \frac{1}{\varepsilon_B} \right) \frac{1}{\gamma} \{ [w_+ \ln(1 - e^{-w_+}) - w_- \ln(1 - e^{-w_-}) - \theta_T [Li_2(e^{-w_+}) - Li_2(e^{-w_-})] \}, \quad (35)$$

$$f_{\text{KN}} = \frac{2(\varepsilon'^2 - 4\varepsilon' - 3)}{\varepsilon(1 + 2\varepsilon')} + \frac{2\varepsilon'}{3} \left[ \frac{4\varepsilon'^2 + 6\varepsilon' + 3}{(1 + 2\varepsilon')^3} \right] - \frac{2(1 + \varepsilon')(\varepsilon'^2 - 2\varepsilon' - 1)}{\varepsilon'(1 + 2\varepsilon')^2} - \left[ \frac{\varepsilon'^2 - 2\varepsilon' - 3}{\varepsilon'^2} \right] \ln(1 + 2\varepsilon') - \frac{2}{\varepsilon'}. \quad (36)$$

In the above expressions,  $w_{\pm} = \varepsilon_{\text{B}}/[\theta_{\text{T}}\gamma(1 - \beta\mu_{\pm})]$ ,  $\varepsilon'_{\pm} = \varepsilon_0\gamma(1 - \beta\mu_{\pm})$  and  $\varepsilon_{\text{B}} = B'$  is the local cyclotron energy in units of  $mc^2$ . Equations (31), (32) and (33) are identical to those given by S95, but the expressions for  $f_{\text{ang}}$ ,  $f_{\text{res}}$  and  $f_{\text{KN}}$  have been generalized to allow for scattering by downward moving particles. Specifically, the corresponding equations given by S95 have specialized to the case of upward moving particles ( $\mu_- = \mu_c, \mu_+ = 1$ , see equation (37) below). equation (34) is the same as D90's equation (16), which is general enough to compute the loss rate of either upward or downward moving particles. Equation (35) includes, to first order, the rest-frame particle recoil  $\varepsilon'_s \simeq \varepsilon'[1 - \varepsilon'(\mu'_s - \mu')^2/2]$  and is a major improvement over previous expressions for resonant Compton scattering that assume no recoil ( $\varepsilon'_s = \varepsilon'$ ). The first term in equation (35) gives D90's equation (54), and the remaining terms result from recoil, where  $Li_2$  is the Dilogarithm function. The treatment of recoil in resonant scattering is necessary in this calculation to compute accurate energies for photons scattered by the electrons and positrons.

Given the generality of the above expressions, the only difference in computing scattering loss rates for upward-moving electrons and downward-moving positrons lies in the integration limits over polar angle  $\mu$  in the laboratory frame. For the case of semi-isotropic blackbody radiation at height  $h = s + h_0$  above a hot PC of radius  $R_{\text{T}}$ , this translates into the following values for

$$\begin{aligned} \text{electrons:} \quad \mu_- &= \mu_c \\ \mu_+ &= 1 \end{aligned} \quad (37)$$

$$\begin{aligned} \text{positrons:} \quad \mu_- &= -1 \\ \mu_+ &= -\mu_c \end{aligned} \quad (38)$$

where

$$\mu_c = \cos \theta_c = \frac{h}{\sqrt{h^2 + R_{\text{T}}^2}}, \quad (39)$$

(when  $R_{\text{T}} \ll R$ ) gives the dilution factor that is present in the soft photon density,

$$n_{\text{ph}}(\varepsilon) = n_{\text{bb}}(\varepsilon) \left( \frac{1 - \mu_c}{2} \right) \quad (40)$$

where

$$n_{\text{bb}}(\varepsilon) = \frac{8\pi}{\lambda_C^3} \frac{\varepsilon^2}{[\exp(-\varepsilon/\theta_{\text{T}}) - 1]} \quad (41)$$

is a blackbody spectrum of temperature  $\theta_{\text{T}}$  and  $\lambda$  is the electron Compton wavelength.

To determine the energy of the scattered photons that may produce pairs, the scattering kinematics of the electron and positron must be treated accurately. For non-resonant scattering in

the Thomson limit, i.e. when  $4\gamma\varepsilon_0 < 1$ , we can assume there is no recoil in the particle rest frame, and the maximum scattered energies in the laboratory frame are

$$\begin{aligned}\varepsilon_s &= 2\gamma^2(1 - \mu_c)\varepsilon_0 && \text{electrons,} \\ \varepsilon_s &= 4\gamma^2\varepsilon_0 && \text{positrons.}\end{aligned}\tag{42}$$

Since the electrons and the soft photons are both moving away from the NS surface,  $\varepsilon_s$  depends on  $\mu_c$ , which decreases with height. However, the positrons scatter the soft photons “head-on” with a maximum angle of  $\pi$ , and  $\varepsilon_s$  is independent of height. When  $4\gamma\varepsilon_0 > 1$ , or for resonant scattering, we must include recoil in the rest frame to compute the scattered energies. The average scattered energy in the laboratory frame is computed from the scattering rates, which for  $\dot{\gamma}_{\text{res}}$  (equation [32]) and  $\dot{\gamma}_{\text{KN}}$  (equation [33]) explicitly include recoil, and the loss rates, so that

$$\langle \varepsilon_s \rangle \approx \frac{\dot{\gamma}_{\text{IC}}}{R_{\text{IC}}}\tag{43}$$

for each component, where

$$R_{\text{IC}} = \frac{c}{\mu_+ - \mu_-} \int_0^{[\gamma(1-\beta\mu_-)]^{-1}} d\varepsilon n_{\text{ph}}(\varepsilon) \int_{\mu_-}^{\mu_+} d\mu (1 - \beta\mu) \int_{-1}^1 d\mu'_s \int_0^{\varepsilon'_{s,\text{max}}} d\varepsilon'_s \left( \frac{d\sigma'}{d\mu'_s d\varepsilon'_s} \right).\tag{44}$$

$\langle \varepsilon_s \rangle$  is thus the weighted average of  $(\varepsilon_s - \varepsilon)$ , where  $(\varepsilon_s \gg \varepsilon)$  for scattering by relativistic particles. Since photons scattered by the “angular” part of the cross section below the resonance do not have energies above pair threshold, for our calculation we need only  $R_{\text{res}}$  and  $R_{\text{KN}}$ . Using equation (44) and following Dermer’s (D90) method of computing  $\dot{\gamma}_{\text{res}}$ , we have

$$R_{\text{res}} = 2.18 \times 10^{13} \left( \frac{T_6 B_{12}}{\beta\gamma^2} \right) \ln \left( \frac{1 - e^{-w_+}}{1 - e^{-w_-}} \right) \text{ s}^{-1}.\tag{45}$$

For  $\gamma \gg 1$ , the resonant scattered photon energy,  $\varepsilon_s^{\text{res}} \simeq \gamma B'$  is independent of incident angle, and is thus the same for upward and downward moving particles. However, the energy of the incident photon in the particle rest frame,  $\varepsilon'_\pm = \varepsilon_0\gamma(1 - \beta\mu_\pm)$  will not be the same, so the upward and downward moving particles will not necessarily both undergo resonant scattering. Using equation (44) and following Sturmer’s (S95) method of computing  $\dot{\gamma}_{\text{KN}}$ , we have

$$R_{\text{KN}} = 3.7 \times 10^{11} \left( \frac{T_6}{\beta\gamma^2} \right) \int_{\varepsilon'_-}^{\varepsilon'_+} d\varepsilon' r_{\text{KN}} \text{ s}^{-1},\tag{46}$$

where

$$r_{\text{KN}} = \frac{4}{\varepsilon'} + \frac{2\varepsilon'(1 + \varepsilon')}{(1 + 2\varepsilon')^2} + \frac{(\varepsilon'^2 - 2\varepsilon' - 2)}{\varepsilon'^2} \ln(1 + 2\varepsilon').\tag{47}$$

Our numerical calculations show that  $\langle \varepsilon_s^{\text{KN}} \rangle$  approaches  $\gamma$  for  $4\gamma\varepsilon_0 \gg 1$ , as expected. Thus,  $\langle \varepsilon_s^{\text{KN}} \rangle > \langle \varepsilon_s^{\text{res}} \rangle$  for  $B' < 1$ .

### 2.3. Pair Production

The method we use to compute the electron-positron pair attenuation length of the photons,  $S_p(\varepsilon)$ , has been described in detail in Harding et al. (1997). Using equation (3),  $S_p(\varepsilon)$  is computed by integrating the pair production attenuation coefficient of the photon along its path through the dipole field. The photon is assumed to pair produce at the point where  $\tau(\theta, \varepsilon) = 1$ , and  $S_p(\varepsilon)$  is then set to that path length. The two main inputs needed are the energy of the photon and its angle to the magnetic field,  $\theta_{\text{kB}}$ . The energies of the radiated photons were given in Sections 2.2.1 and 2.2.2. For the angle of the radiated photons at the emission point, we assume that  $\theta_{\text{kB}} = 2/\gamma$  for Compton scattered photons (D90) and  $\theta_{\text{kB}} = 0$  for CR photons. Due to the curvature of the field lines,  $\theta_{\text{kB}}$  will grow as the photon propagates, roughly as  $\sin \theta_{\text{kB}} \sim s/\rho_c$ . To evaluate the pair production attenuation coefficient at each point along the path of the photon, we Lorentz-transform the photon energy and local magnetic field to the frame in which the photon propagates perpendicular to the local field. This is the center-of momentum frame for the created pair, where the attenuation has its simplest form and the photon energy is  $\varepsilon_{\text{CM}} = \varepsilon \sin \theta_{\text{kB}}$ . The one-photon pair attenuation coefficient is considered in two regimes. For  $B < 0.1 B_{\text{cr}}$ , photon pair produce far above threshold, where the asymptotic expression in the limit of large numbers of kinematically available pair Landau states (Tsai & Erber 1974, DH83) can be used:

$$T_{\parallel, \perp}^{\text{pp}} = \frac{1}{2} \frac{\alpha}{\lambda} B' \Lambda_{\parallel, \perp}(\chi), \quad (48)$$

$$\Lambda_{\parallel, \perp}(\chi) \approx \begin{cases} (0.31, 0.15) \exp\left(-\frac{4}{3\chi}\right) & \chi \ll 1 \\ (0.72, 0.48) \chi^{-1/3} & \chi \gg 1 \end{cases} \quad (49)$$

where  $\chi \equiv f \varepsilon_{\text{CM}}/2B'$ ,  $\alpha$  is the fine-structure constant,  $B'$  is the dipole field strength at point  $s$  along the photon path (see equation [28]). When  $B > 0.1 B_{\text{cr}}$ , pair production will occur near threshold, where the above expression is not accurate. We thus include the factor  $f = 1 + 0.42\varepsilon_{\text{CM}}^{-2.7}$  in  $\chi$ , introduced by DH83, as an approximation to the near-threshold attenuation coefficient. In this paper we compute the attenuation length averaged over photon polarization.

### 2.4. Backflowing Positrons, Double Pair-fronts and Polar Cap Heating

Soon after the concept of electron-positron pair production had been introduced into pulsar models (Sturrock 1971), it became clear that the precipitation of positrons (or, in some models, electrons) onto the stellar surface may have some important effects. For example, Sturrock has noticed that (see p. 531) “if the positrons were all returned to the surface, the resulting space charge would reverse the sign of the electric field at the surface, cutting off the flux of primary electrons”. Then he added that “one possibility is that the configuration so adjusts itself that the primary flux is never quite cut off, so that the flow is steady, and another possibility is that

the flow is oscillatory”. Thus, he drew attention to the existence of an intrinsic feedback between the pair formation and the electric field accelerating primary particles. Later on, several authors (see e.g. RS75, Jones 1978, AS79, and Arons 1981) have discussed similar ideas focusing on the possibility of PC heating by the flow of energetic positrons (electrons). DH96 discussed the effect of downward moving positrons on the particle acceleration and the possibility of a lower PFF. The most detailed study has been performed by AS79 who calculated the fraction of returning positrons, structure of the PFF with positron trapping near but below the lower boundary of the PFF, and briefly discussed the positron-initiated cascade very near the stellar surface. They estimated the fraction of returning positrons as  $\sim \theta_0^2$  ( $\ll 1$ , where  $\theta_0$  is the half-opening angle of the polar flux tube at the stellar surface) of the Goldreich-Julian charge density. The main argument underlying this estimate is that the contribution of the second term in the square bracket in equation (4) increases with altitude (due to the flaring of the magnetic field lines emanating from the PC), and that (see AS79, p. 867) “the additional negative charge density needed to achieve  $E_{\parallel} = 0$ , over and above that of the electron beam, is therefore a fraction  $\sim \theta_0^2$  of the negative charge density already present in the electron stream”. And, “as the pairs begin to form near but below some height (at which the electric field shuts off), the residual  $E_{\parallel}$  of the diode causes the secondary electron-positron plasma to polarize and shield these “external” charges. The formation of this polarization charge requires a dynamical response which, under most conditions, leads to the formation of the downward directed positron stream whose flux at the stellar surface is  $F_+ \ll F_-$ ”. However, the main problem with this reasoning is that if we assume the zero-electric field boundary condition at the stellar surface, then “the additional negative charge density” is nothing else but the imbalance between the real and Goldreich-Julian charge densities that produces the electric field above the stellar surface in the first place. This imbalance (or charge deficit) increases with altitude and reaches some maximum value. Thus, if the backflowing positrons shield these “external” charges at some height, then they will also screen the electric field all the way down to the stellar surface, and we should unavoidably come up with the situation envisaged by Sturrock, where the returning positrons cut off the flux of primary electrons, thus resulting in the oscillatory regime.

In this section, we explore the possibility of occurrence of a steady regime of positron backflow that is not capable of disrupting the current of primary electrons. We also discuss the efficiency of PC heating produced by the precipitating relativistic positrons and high-energy quanta. We also discuss the accounting of the feedback between the returning positron flux and electric potential distribution in the acceleration region in the self-limiting regime of particle flow. The primary (electron) traversing the region of the electric potential drop emits a  $\gamma$ -ray photon that produces an electron-positron pair at the altitude  $h_{\text{pair}}$  above the stellar surface. The electron-positron pairs keep moving forward, with some positrons of these pairs decelerating and eventually reversing the direction of their motion at some altitude  $h_c$ . It is very likely that the same effect tends to occur with the positrons from both additional photons emitted by the same electron or from a second generation of pairs. An accurate determination of the fraction of backflowing positrons would require a self-consistent calculation of the screening of  $E_{\parallel}$  by the cascade pairs and the



modification of the pair energy and spatial distribution by the screened  $E_{\parallel}$ . Short of carrying out such a detailed calculation here, we shall derive an upper limit on the fraction of returning positrons. However, since the cascades develop very fast and the number density of particles increases in an avalanche, the altitudes at which the positrons from the higher-order cascades get decelerated should be very close to but slightly above  $h_c$ . The deceleration of positrons results in a charge separation in the initially quasi-neutral electron-positron beam, thus effectively shielding the electric field where the bulk of the pair front is produced. We can justifiably assume that  $E_{\parallel} = 0$  at  $h \approx h_c$ . The backflowing positrons slightly suppress the voltage all the way down to the bottom of the polar magnetic flux tube, so that the electric field  $E_{\parallel}$  (and also potential  $\Phi$ ) vanishes at a height greater than the start-off height of the primary electrons. This occurs because the flux of backflowing positrons is equivalent to a corresponding enhancement of the total electron current and therefore of the maximum number of electrons per second to be ejected into the acceleration region. Thus, in compliance with the zero-electric field boundary condition, the ejection radius should fix itself at the larger value corresponding to a higher effective “rate of supply of Goldreich-Julian charge” (see also expressions [4] and [51] proving this statement).

Let us introduce the Goldreich-Julian current (associated with the corresponding charge density) or the rate of ejection of charges per element of the solid angle into the region of open magnetic field lines

$$\frac{d\mathcal{I}_{\text{GJ}}}{d\Omega_{\xi}} = \alpha c |\rho_{\text{GJ}}|(r\theta)^2, \quad (50)$$

where  $(r\theta)^2 \equiv (\Omega R/c)R^2\eta^3\xi^2/f(\eta)$ , and  $d\Omega_{\xi} = \xi d\xi d\phi$  is an element of the solid angle in the PC region. In the rest of this Section we present our estimate of the maximum power carried by the backflowing positrons. Using the general-relativistic expression for  $\rho_{\text{GJ}}$  (equation [11]) we can write

$$\frac{d\mathcal{I}_{\text{GJ}}(\eta_{\text{E}})}{d\Omega_{\xi}} = \frac{\mathcal{I}_0}{2\pi} \left[ \left( 1 - \frac{\kappa}{\eta_{\text{E}}^3} \right) \cos \chi + \frac{3}{2} H(\eta_{\text{E}}) \theta(\eta_{\text{E}}) \xi \sin \chi \cos \phi \right], \quad (51)$$

where  $\mathcal{I}_0 \equiv (\Omega R/c)^2 B_0 R c / f(1)$  and  $\eta_{\text{E}} \equiv R_{\text{E}}/R \equiv (R + h_0)/R = 1 + h_0/R > \eta$ .

The zero-electric field boundary condition at  $\eta = 1$  requires the magnitude of the primary electron current flowing from the PC surface to be equal to  $(d\mathcal{I}_{\text{GJ}}/d\Omega_{\xi})|_{\eta=\eta_{\text{E}}}$ . This expression implies (compare with expression [4]) that an enhanced electron current is ejected from the effective radius in the regime of self-limitation or, equivalently, allows for the additional current of positrons flowing from the upper PFF downward. It is important that in the steady-state regime the total current of actual charges (electrons and positrons) remains constant along the field lines, and is fixed by the Goldreich-Julian current at the zero-electric field boundary (i.e., in our case, at the effective radius  $R_{\text{E}}$ ). The electric field above  $R_{\text{E}}$  (in the regime of self-limitation) is produced by the imbalance between the actual current and the local value of the Goldreich-Julian current. At distances greater than the effective radius  $R_{\text{E}}$  for the Goldreich-Julian current we can write

$$\frac{d\mathcal{I}_{\text{GJ}}(\eta > \eta_{\text{E}})}{d\Omega_{\xi}} \approx \frac{\mathcal{I}_0}{2\pi} \left[ \cos \chi + \frac{3}{2} H(\eta) \theta(\eta) \xi \sin \chi \cos \phi \right]. \quad (52)$$

Let us consider the situation when the fraction of positrons returning from the upper PFF is not only sufficient to produce a lower PFF, but is also big enough to affect the electric field accelerating the primary electrons. For example, the backflowing positrons tend to reduce the accelerating electric field above the effective surface of radius  $R_E$ , simply because the positron current is equivalent to the enhanced electron current which unavoidably requires the electrons to be ejected from the greater heights above the effective surface. Thus, the returning positrons may eventually screen the accelerating electric field and trigger an oscillating regime with alternating phases of developing and collapsing of double pair fronts. As has been mentioned above, the oscillatory regime akin to that we discuss here was anticipated in his classical paper by Sturrock (1971), even though he did not discuss the lower PFF. The occurrence of the oscillatory regime depends on the fraction of backflowing positrons, which is determined by the particle kinematics within the upper PFF and the penetration depth of the electrostatic field into the electron-positron plasma cloud. A quantitative description of this process would be possible through a detailed analysis of the electron-positron cascades and their feedback on the electrodynamics of the pair formation region. We can now estimate the maximum positron current needed to screen the electric field accelerating the primary electrons. For this purpose we assume that the bulk of the lower pair front sets up at the effective radius  $R_E$ , and that the upper pair front establishes at the radial distance  $r > R_E$ . Then, for the maximum positron current we can write, using equations (51) and (52),

$$\left(\frac{d\mathcal{I}_{e^+}}{d\Omega_\xi}\right)_{\max} \approx \frac{d}{d\Omega_\xi} [\mathcal{I}_{GJ}(\eta > \eta_E) - \mathcal{I}_{GJ}(\eta_E)] = \frac{\mathcal{I}_0}{2\pi} \left[ \kappa\eta_*^3 \cos \chi + \frac{3}{2}H(\eta)\theta(\eta)\xi \sin \chi \cos \phi \right], \quad (53)$$

where  $\eta_* \equiv R/R_E$ . The maximum value of the electric potential can be estimated as (cf. equation [13])

$$\Phi_{\max} \approx \frac{\mathcal{I}_0}{2c} \eta_* \left[ \kappa\eta_*^2 \cos \chi + \frac{3}{4}H(\eta)\theta(\eta)\xi \sin \chi \cos \phi \right] (1 - \xi^2). \quad (54)$$

Now we can derive the maximum total power put into the backflowing positrons (cf. MH97, equations [76]-[78]):

$$\{L_{e^+}\}_{\max} \approx \int_{\Omega_\xi} \Phi_{\max} \{d\mathcal{I}_{e^+}\}_{\max} \approx \{\lambda_+\}_{\max} \frac{\mathcal{I}_0^2}{6c} \equiv \{\lambda_+\}_{\max} L_{\text{sd}}, \quad (55)$$

where

$$\{\lambda_+\}_{\max} = \frac{3}{4}\eta_* \left( \kappa^2\eta_*^5 \cos^2 \chi + \frac{3}{16}H^2\theta^2 \sin^2 \chi \right), \quad (56)$$

and

$$L_{\text{sd}} \equiv \frac{\Omega^4 B_0^2 R^6}{6c^3 f^2(1)} \quad (57)$$

is the spin-down luminosity of a pulsar. A similar estimate for the maximum efficiency of acceleration of primary electrons yields

$$\{\lambda_-\}_{\max} = \frac{3}{4} \left[ \kappa\eta_*^3 (1 - \kappa\eta_*^3) \cos^2 \chi + \frac{3}{16}H^2\theta^2 \sin^2 \chi \right], \quad (58)$$

which amounts to 10 % (for a small obliquity and  $\eta_* \approx 1$ ).

For relatively small obliquities (or small magnetic polar angles and non-orthogonal rotator) and typical pulsar spin periods of 0.1 - 1 s the first term in equation (56) dominates, and we get

$$\{\lambda_+\}_{\max} \approx \frac{3}{4} \kappa^2 \eta_*^6. \quad (59)$$

For a 1.4 solar mass NS and for a broad range of realistic equations of state of dense matter (see e.g. Lorenz, Ravenhall, & Pethick 1993 and Ravenhall & Pethick 1994 for the calculations of the NS moment of inertia for various equations of state)  $I/(MR^2) \approx (0.2 - 0.25)(1 - r_g/R)^{-1}$ . Thus, for the NS of 1.4 solar mass and 8-10 km radius (which is consistent with the most realistic stellar models) we can estimate  $\kappa \equiv (r_g/R)(I/MR^2) \approx 0.15 - 0.27$ . Given  $\eta_* \simeq 0.5 - 1$  (see Section 3.1), equation (59) yields

$$\{\lambda_+\}_{\max} \approx \left(3 \cdot 10^{-4} - 2 \cdot 10^{-2}\right) \left(\frac{\kappa}{0.15}\right)^2. \quad (60)$$

This estimate combined with the recently observed X-ray luminosities (that include both pulsed and non-pulsed components and imply isotropic emission) of pulsars (see Becker & Trümper 1997) may have rather interesting implications. If the X-ray fluxes in some of these pulsars are dominated by the photons from the heated (e.g. by the backflowing positrons) PC, then luminosities higher than given by equation (60) would indicate that these pulsars operate in the oscillatory regime discussed above. According to the estimates by Becker & Trümper the pulsed X-ray luminosities (for the case of isotropic emission),  $L_x^p$ , for e.g. Crab, Vela, Geminga, and PSR 0656+14 are, respectively,  $1.6 \cdot 10^{-3}$ ,  $0.7 \cdot 10^{-5}$ ,  $1.3 \cdot 10^{-4}$ , and  $3.7 \cdot 10^{-3} L_{\text{sd}}$  (where  $L_{\text{sd}} \equiv I\Omega|\dot{\Omega}|$ ,  $\Omega$  and  $\dot{\Omega}$  are the pulsar spin frequency and its time derivative, respectively). Although some of these pulsars have X-ray luminosities that lie above  $\{L_{e^+}\}_{\max}$ , the X-ray emission may not be isotropic (see Zavlin et al. 1995). If we assume that at least for Vela, Geminga, and PSR 0656+14 (see e.g. Harding & Muslimov 1998 for the modeling of the soft X-ray and  $\gamma$ -ray emission for these pulsars) the X-ray emission is beamed into a solid angle of  $\sim 1$  steradian, then for these pulsars we can estimate that  $\{\lambda_x^p\}_{\text{anis}} \equiv \{L_x^p\}_{\text{anis}}/L_{\text{sd}} \sim 6 \cdot 10^{-7}$ ,  $10^{-5}$ , and  $3 \cdot 10^{-4}$ , respectively. The corresponding PC temperature for these pulsars can be estimated as

$$T_{\text{pc}} \sim (0.6 - 1) \cdot 10^6 \left(10^5 \{\lambda_x^p\}_{\text{anis}}\right)^{1/4} \left(\frac{B_0}{4 \cdot 10^{12} \text{ G}}\right)^{1/2} \left(\frac{R}{8 \text{ km}}\right)^{3/4} \left(\frac{P}{0.1 \text{ s}}\right)^{-3/4} \text{ K}. \quad (61)$$

Thus, the estimated value of  $\{\lambda_x^p\}_{\text{anis}} \sim (3 \cdot 10^{-5} - 10^{-2}) \{\lambda_+\}_{\max}$  may indicate that the backflowing positrons precipitate onto the effective area smaller than that of the standard PC (e.g. the returning positrons focus toward the magnetic axis as discussed below), and/or that the fraction of the returning positrons is well below the maximum possible one. Then the latter would support the quasi-steady state (MH97) rather than the oscillatory (Sturrock 1971) regime of pulsar operation.

The energetics of the PC heating is mainly determined by the energetics of the backflowing (primary) positrons. Their energy is eventually redistributed between the high-energy photons

they emit and electron-positron pairs created by photons in the magnetic field. Let us consider the last open field line of the dipole magnetic field. The photons emitted by backflowing positrons produce pairs on adjacent innermost field lines, which may reduce the effective area of the PC subject to the heating. Here we shall present very rough estimate of the geometrical filling factor for the PC heating qualitatively illustrating this effect. The photons emitted by backflowing positron (moving along the last open field line) at height  $S_c^+$  above the effective radius  $R_E$  produces a pair at the effective radius and at the angular distance from the magnetic axis

$$r^* = (R_E + S_c^+) \tan \theta - S_c^+ \tan \lambda, \quad (62)$$

where  $\theta$  is the magnetic colatitude of the point at which the photon is emitted, and  $\lambda$  is the angle between the tangent to the field line at the point of photon emission and the normal to the stellar surface (here we may justifiably neglect the surface curvature). In a flat space limit elementary geometrical consideration yields the relationship  $\lambda = \mu + \theta$ , where  $\mu$  is the angle between the tangent to the field line and the radius-vector of the point on the field line with the magnetic colatitude  $\theta$ . For a dipole field,  $\tan \mu \approx \frac{1}{2} \tan \theta \approx \frac{1}{2} \theta$ , so that  $\tan \lambda \approx \frac{3}{2} \theta$ , and we get

$$r^* = R_E \left( 1 - \frac{S_c^+}{2R_E} \right) \theta. \quad (63)$$

Since  $\theta = \theta_{\text{pc}} [(R_E + S_c^+)/R]^{1/2}$ , where  $\theta_{\text{pc}}$  is the angular size of a standard PC, we can write for the effective angular size (at the actual stellar radius) of the heated PC

$$\theta^* = \theta_{\text{pc}} \left( 1 + \frac{S_c^+}{R_E} \right)^{1/2} \left( 1 - \frac{S_c^+}{2R_E} \right). \quad (64)$$

Thus, in the case where  $S_c^+ \sim R$ , and  $R_E \sim (1 - 2)R$ , we get

$$\theta_{\text{pc}}^* \approx (0.7 - 0.9) \theta_{\text{pc}}.$$

The effective area of the heated PC may therefore be up to 50 % less than the area of a standard PC. The above estimate can be additionally justified by the fact that  $S_c^+$  increases toward the PC rim, while  $R_E$  remains practically constant. We thus suggest that for some pulsars this effect may be worthy of discussion.

### 3. Self-Limited Acceleration Zone

#### 3.1. Numerical Results

Following the procedure outlined in Sections 2.1-2.3, we have made numerical calculations of the PFFs and the total acceleration length,  $S_c$ , from equation (1), for both upward moving electrons and downward moving positrons. The parameters of the thermal radiation from the NS

surface are somewhat uncertain. Although measured temperatures of pulsed X-rays lie in the range  $5 \times 10^5 - 10^6$  K, the distribution of the radiation is not known. For the calculations of this Section, we have assumed that the radiation is isotropically emitted from a hot PC of radius  $R_T = 3\theta_0 R$  and that  $R = 8$  km. Other possibilities, and how they might affect these results will be discussed in Section 4. An electron is started at height  $h_0$  above the NS surface with  $\gamma^- = 1$ . For a given value of  $h_0$  and thus,  $R_E = R + h_0$ , a “first guess” value of  $h_c$ , and thus also of  $S_c^-$ , sets the initial acceleration length. equation (2) is integrated in discrete steps upward from the starting point, computing  $E_{\parallel}$  (from either equation [18] or [23]),  $\dot{\gamma}_{\text{IC}}$  and  $\dot{\gamma}_{\text{CR}}$  at each step. At each step, the pair attenuation lengths,  $S_p(\varepsilon)$ , of both CR and ICS test photons radiated by the particle of energy  $\gamma(s)$  are computed from equation (3). The pair attenuation length, and thus the value of  $S_c^-$ , also computed at every step, is initially infinite, because the energy of the photons is small, but decreases with distance as the energy of the radiated photons increases. Although the photon attenuation length continues to decrease, the particle acceleration length is increasing and  $S_c^-$  has a minimum. This minimum value of  $h_c = h_0 + (S_c^-)_{\text{min}}$  is adopted as the new value of the electron PFF for the assumed value of  $h_0$ . The electron is accelerated again with the new value of  $h_c$ , producing a new PFF at the next value of  $h_c = h_0 + (S_c^-)_{\text{min}}$ . The process is repeated, converging to a self-consistent value of  $h_c$ .

When  $h_0 \ll R$ , we find that the value of  $S_c^-$  for ICS photons is smaller than that for CR photons. PFFs at low altitudes are therefore ICS-controlled. Figure 2 shows examples of self-consistent solutions of the ICS-controlled electron PFF near the NS surface (left panel) and the corresponding ICS-controlled positron PFF (right panel). In the left panel of Fig. 3, an electron starts very near the NS surface (at height  $h_0 = 0.01 R$ ), where the density of soft thermal photons and the loss rate due to ICS is high. In this case, photons from resonant ICS produce pairs well before CR photons and thus the ICS photons establish the PFF. In fact, the loss rate for CR is orders of magnitude smaller than that for ICS at the PFF. In the right panel of Fig. 2, the loss rates and integrated energy of the positron, accelerated by the same electric field as the electron, is shown as a function of the acceleration length. In this case, however, the larger angles between the thermal X-ray photons and the positrons allow them to accelerate through the resonant part of the ICS losses at lower energies, and non-resonant ICS of photons above the cyclotron energy produce the PFF. Since at pulsar field strengths, scattering above the cyclotron energy occurs in the KN regime, the scattered photon energies are much larger than those of photons scattered in the resonance. Therefore, the ICS photons producing the positron PFF have higher energies than the ICS photons producing the electron PFF (see Fig 7) and the positron PFF forms in a shorter distance. This is the major cause of the difference between the electron and positron ICS-controlled PFFs, which will be discussed in more detail in connection with Fig. 8. Figure 3 shows an example of the self-consistent solution for a CR-controlled electron PFF. The electron begins accelerating at a significant fraction of a stellar radius above the surface, where the soft photon density has dropped, CR losses dominate and CR photons establish the PFF. Because CR is much less efficient than ICS, the particles must accelerate to higher energies to produce pairs and the total acceleration length  $S_c$  is longer.

We first explore the solutions for the electron PFF, as a function of pulsar parameters, for acceleration from the surface. Figures 4 and 5 show the height of the electron PFF and the maximum acceleration voltage ( $\gamma_{\max}$ ) as a function of the scaled colatitude  $\xi$  for CR-controlled PFFs, assuming that ICS is “turned off”. These results can be directly compared with Fig. 5 of A83, who computed the PFF due only to curvature photons. Figure 4 shows the strong effect of obliquity  $\chi$  on the shape of the electron PFF and on the acceleration voltage, due primarily to the dependence of  $E_{\parallel}$  on  $\chi$ . Since the frame-dragging component of  $E_{\parallel}$  proportional to  $\cos \chi$  (cf. equation [18]) is much stronger near the surface than the component proportional to  $\sin \chi$ , it dominates at small and intermediate values of  $\chi$ . The frame-dragging electric field becomes comparable to that in a flat space for orthogonal rotators ( $\chi = 90^{\circ}$ ), where our solutions match very well with those of A83’s Fig. 5. The height of the CR-controlled PFF ( $S_c^-$ ) increases and  $\gamma_{\max}$  decreases with increasing  $\chi$ , as  $E_{\parallel}$  decreases. The height of the PFF increases sharply (and in fact goes to infinity) both at the magnetic pole ( $\xi = 0$ ) and at the PC rim ( $\xi = 1$ ). These features, referred to as slot gaps by Arons, form at the pole and equator due to different effects. The gap at the pole occurs because the radius of curvature of the magnetic field lines is infinite there, causing the pair attenuation length to go to infinity. The electrons keep accelerating to high altitudes and thus reach high energies. At the PC rim, the boundary condition on the potential ( $\Phi = 0$ ), screens  $E_{\parallel}$  close to the rim, preventing electron acceleration to high enough energy to produce any pairs. Thus,  $\gamma_{\max}$  also goes to zero at the rim. Figure 5 shows the dependence of the PFF height and acceleration voltage on surface magnetic field strength  $B$ . While the height of the PFF decreases with increasing  $B$ , due both to an increase in  $E_{\parallel}$  and a decrease in pair attenuation length,  $\gamma_{\max}$  is roughly constant even though  $B$  varies over two decades. This is because the longer total acceleration distance for lower field strengths compensates for the lower rate of acceleration.

Figure 6 shows examples of ICS-controlled PFFs near the NS surface. We find that both the height of the PFF and the acceleration voltage is much lower than for the CR-controlled PFFs. This is due to the higher efficiency of ICS in producing photons of pair-producing energy. ZQLH97 obtained a similar result for ICS-controlled PFFs using the electric field of RS95. Electrons having Lorentz factors of only  $10^5 - 10^6$ , depending on  $\xi$ , are capable of radiating photons of about 10% to almost 100% of their energy, and these photons will produce pairs. Again, the maximum Lorentz factor,  $\gamma_{\max}$ , is a very weak function of field strength. The ICS-controlled PFF height, however, behaves very differently near the magnetic pole. Instead of forming a slot gap, like the CR-controlled PFFs, the height of the PFF actually decreases near the pole. ICS photons are radiated at much larger angles to the field and thus have shorter pair attenuation lengths than curvature photons.

The above determinations of the electron PFF are not fully self-consistent in that they have neglected pairs produced by the positrons that slow down to screen  $E_{\parallel}$  and accelerate down toward the stellar surface. Even if the number of returning positrons is small compared to the number of primary electrons, the multiplicity of the downward cascades is high (DH96), due to the increasing field strength. From our simulations of downward going cascades using the code of DH96, we find

that the multiplicity of a positron accelerated toward the PC from a height of one stellar radius at the PC rim is  $M_p \sim 10^4 - 10^5$ . If the fraction of positrons that are accelerated downward from the electron PFF is  $f_p = \lambda_+/\lambda_- \sim 3 \times 10^{-3} - 2 \times 10^{-1}$  (see equations [58] and [56]), then there are  $f_p M_p \sim 30 - 2 \times 10^3$  pairs produced by downward cascades for each primary electron. This would seem to be sufficient to screen  $E_{\parallel}$  and form a lower PFF.

To compute the location of the lower PFF, a test positron is started at the upper (electron) PFF with an energy of  $\gamma^+ = 1$ . In reality, there is a spread in energies of the pairs created near the electron PFF, so that the most energetic ones will decelerate but not turn-around, while the less energetic ones will decelerate before they reach the PFF and accelerate downward with varying initial energies. We have thus neglected the detailed kinematics of this turn-around process. Equation (2) is then integrated to follow the downward acceleration of the positron and its energy losses due to both ICS and CR, in the same manner as for the electron. Likewise, the attenuation lengths of the photons and the total acceleration length of the positron are computed. Although the PFFs of the positrons, like the electrons, are produced by pairs from the ICS process near the NS surface in the presence of thermal radiation from a hot PC, we find that the positron PFF is always above the start of the electron acceleration. That is, pair front formation by the ICS process is not symmetric for upward and downward going particles. This is because the positrons scatter the thermal photons at much larger angles than the electrons. While the ICS photons producing the electron PFF scatter in the cyclotron resonance to an energy of  $\sim \gamma B'$ , photons producing the positron PFF scatter above the cyclotron resonance, in the KN regime (see Fig. 2), where the scattered energy is  $\sim \gamma$ . This asymmetry will occur for field strengths  $B' \lesssim 0.5$ , above which positrons will form PFFs through resonant ICS. As discussed further in Section 3.2, stable ICS-controlled double PFFs may exist for high-field pulsars because the scattered energy for resonant scattering is independent of incident angle. Figure 7 shows the difference between the electron,  $\gamma_{\min}^-$ , and positron,  $\gamma_{\min}^+$ , energies that produce scattered photons of energy  $\varepsilon_{\min}^+$  and  $\varepsilon_{\min}^-$  that form the minimum PFFs, as a function of  $h_0$ . Since their ICS is more inefficient, the electrons must accelerate to much higher energies in order to produce scattered photons that pair-produce. The efficiency of electron scattering,  $\varepsilon_{\min}^-/\gamma_{\min}^-$ , decreases with height,  $h_0$ , above the surface, while the efficiency of positron scattering increases. Therefore, the positrons are able to radiate pair-producing photons after traveling a shorter acceleration path. Since the scattered energies of the positrons, at a given height, are greater than those of the electrons, these photons have shorter pair attenuation lengths. Thus, the total positron acceleration length,  $S_c^- = S_a(\gamma_{\min}^-) + S_p(\varepsilon_{\min}^-)$  is less than the total electron acceleration length,  $S_c^+$ .

Figure 8 shows total positron and electron acceleration lengths,  $S_c^+$  and  $S_c^-$  as a function of the electron starting height  $h_0$ , for both ICS- and CR-controlled PFFs. In these calculations, we have allowed the self-consistent PFFs of electrons and positrons to form with only one of the radiation mechanisms operating. When only ICS produces pairs,  $S_c^+$  is always significantly less than  $S_c^-$  and the difference increases with height. However, when ICS is suppressed and only CR is allowed to operate,  $S_c^+$  and  $S_c^-$  are equal. That is because CR for electrons and positrons is

the same, the only difference being in radius of curvature between the radiation points, which is negligible since  $S_c^- \ll R$ . While ICS cannot provide self-consistent solutions to the double PFFs, CR can. We suggest that stable, self-consistent double PFFs can only exist when they are formed by CR. Since ICS will dominate near the surfaces of NSs radiating thermal soft X-rays, evidence of which has been observed in many pulsars, stable PFFs can only form at a height above the surface where CR becomes dominant. We take a rough estimate for the height of CR-control of the electron and positron PFFs to be where CR energy loss of the electrons dominates over ICS energy loss. If electrons of energy  $\gamma_{\min}^-$  radiate more curvature photons than ICS photons, then the ICS PFF will disappear, and the electrons will continue accelerating until a curvature PFF is established. When the positrons accelerating downward from the electron curvature PFF also establish curvature photon PFFs, then stable acceleration can occur. In reality, the PFFs will switch from ICS to CR control when the number of pairs produced by ICS photons becomes too small to screen  $E_{\parallel}$ . But to determine the number of pairs necessary for establishing a lower PFF, we would need to know the number of returning positrons. Figure 9 shows an example of the electron energy loss rates due to ICS and CR at energy  $\gamma_{\min}^-$  as a function of height of the lower PFF. At low altitudes, ICS losses dominate by many orders of magnitude, but decrease with  $h_0$  mostly due to the decrease in the thermal photon density (cf. equation [40]). The energy  $\gamma_{\min}^-$  of electrons that are forming the ICS PFF increase with altitude due to the decreasing efficiency of ICS. Their CR losses, which are a strong function of energy, therefore increase. The height at which electron ICS and CR losses are equal, which roughly set the location of stable acceleration, will depend on the PC thermal temperature and radius (cf. equation [76]).

We have computed the height of the stable acceleration zones where CR losses dominate control of PFFs for various pulsar parameters. As shown in Figure 10, the location of the lower (positron) PFFs  $h_0$  are at higher altitudes for higher surface magnetic field strengths, because the ICS losses are proportional to  $B^2$  for resonant scattering. The height of the lower PFF decreases for increasing pulsar rotation period,  $P$ , because at a given colatitude  $\xi$  the radius of curvature increases, but the electron energy  $\gamma_{\min}^-$  increases so that CR can dominate at a lower altitude. Figure 11 shows the width of the CR-controlled acceleration zone,  $S_c^-$  (i.e. the distance between the lower and upper curvature PFFs) and the maximum voltage drop,  $\gamma_{\max}$ , as a function of pulsar period and surface field strength. The maximum particle energy is again remarkably insensitive to pulsar parameters, even though the acceleration zone width shows substantial variation. The width  $S_c^-$  tends to be smaller for larger fields because both the acceleration length and the pair attenuation length are shorter. It has a large increase at long periods, where the pair attenuation lengths become large due to the increase in the PC radius of curvature. In fact, there will be a maximum period for which electron PFFs can form at a given colatitude.

Figure 12 shows solutions for the width and maximum Lorentz factor of the self-consistent, stable acceleration zones that are controlled by CR double PFFs. The width of these zones, located nearly a stellar radius above the surface, are larger than CR-controlled zones at the surface (e.g. Fig. 4 and 5), because the magnetic field has fallen from its surface value, so that



$E_{\parallel}$  is lower, and the radius of curvature is larger. However, the maximum Lorentz factor of the higher altitude acceleration zones is roughly the same as that at the surface. Again, the size of the acceleration path has adjusted itself to maintain the same maximum energy, which depends only on the geometry of the magnetic field.

### 3.2. Analytic Estimates

It is difficult to derive accurate analytic expressions for the acceleration zone parameters we have computed numerically, such as height and width of the stable acceleration zone. The form of the electric field changes as a function of acceleration length (see Appendix), starting as a linear function and then saturating at  $s \sim R_{\text{pc}}$  to become a constant. Consequently, there are no simple expressions for the processes that apply for altitudes from the surface to several stellar radii. Nevertheless, we can characterize the behavior of the solutions in different regions. An estimate for  $h_0$ , the height at which control of the PFF formation switches from ICS to CR, can be obtained by finding the height at which the loss rates for CR and ICS of positrons with energy  $\gamma_{\text{min}}$  are equal:

$$\dot{\gamma}_{\text{IC}}(\gamma_{\text{min}}) = \dot{\gamma}_{\text{CR}}(\gamma_{\text{min}}). \quad (65)$$

We can obtain an estimate of  $\gamma_{\text{min}}$  by solving equation (1). For  $s \lesssim 3R_{\text{pc}}$ , we can use the expression for  $E_{\parallel}$  given in equation (A3) of the Appendix, which is linear in  $s = zR_E$  and thus gives a quadratic energy increase in particle energy with  $s$ . The particle acceleration length is then:

$$S_a(\gamma) = (\gamma/A_{\gamma})^{1/2} \quad (66)$$

where

$$A_{\gamma} \simeq \left( \frac{3e}{2mc^2} \right) \left( \frac{\Omega R}{c} \right) \frac{B_0}{1 - \epsilon} \left( \frac{\kappa}{R_E} \right) \left( \frac{R}{R_E} \right)^2 \cos \chi. \quad (67)$$

Note that we have rescaled equation (A3) to the effective radius  $R_E$ , at which the acceleration begins. The pair attenuation length can be approximated as the mean free path

$$S_p(\epsilon) \simeq \left( \frac{0.2\rho_c}{B'\epsilon} \right) \quad (68)$$

valid for  $B' \lesssim 0.1$ . Equation (1) may then be written,

$$S_c = \min \left\{ (\gamma/A_{\gamma})^{1/2} + \frac{0.2\rho_c}{B'\epsilon} \right\}, \quad (69)$$

where

$$\rho_c \simeq \frac{4}{3} R_E^{1/2} \left( \frac{\Omega}{c} \right)^{1/2} \quad (70)$$

and

$$B' \simeq \left( \frac{B_0}{B_{\text{cr}}} \right) \left( \frac{R_E}{R} \right)^{-3}. \quad (71)$$

We wish to estimate  $\gamma_{\min}$  when ICS produces the PFFs. For nearly all pulsar field strengths ( $B \lesssim 0.5 B_{\text{cr}}$ ) the photons which produce the positron PFFs have been blue-shifted above the resonance and scatter in the KN regime (see Fig. 2). In this case, we can approximate the scattered photon energy as  $\varepsilon \sim \gamma$ . Inserting this value of  $\varepsilon$  into equation (69), we then obtain  $\gamma_{\min}$  giving the minimum  $S_c$  by setting the derivative of  $S_c$  with respect to  $\gamma$  to zero:

$$\gamma_{\min}^{KN} = \left( \frac{0.4 \rho_c A \gamma^{1/2}}{B'} \right)^{2/3} = 3.4 \times 10^5 B_{12}^{-1/3} \left( \frac{R_E}{R} \right) (\cos \chi)^{1/3}. \quad (72)$$

where  $B_{12}$  is the surface field strength. Thus, the particle energy required to radiate pair-producing photons increases with altitude, as was found in our numerical results (cf. Fig. 7).

We can obtain an estimate for the width of the ICS controlled acceleration zones by substituting  $\gamma_{\min}^{KN}$  from equation (72) into equation (69) for the minimum value of  $S_c$ ,

$$S_c^{KN} \simeq 5.3 \times 10^3 B_{12}^{-2/3} P^{1/2} R_6^{1/2} \left( \frac{R_E}{R} \right)^{5/2} (\cos \chi)^{-1/3} \text{ cm}. \quad (73)$$

We can estimate the height  $h_0$  above the surface at which CR energy loss exceeds ICS losses for the downward moving positrons of energy  $\gamma_{\min}$ . From our numerical results, we found that at the altitudes where CR begins to dominate the particle energy loss, the ICS is in the K-N regime above the resonance. We will therefore equate the curvature loss rate to the K-N loss rate to obtain an estimate for  $h_0$ . Substituting  $\gamma_{\min}$  from equation (72) in equation (25) for the CR energy loss, we have

$$\dot{\gamma}_{\text{CR}}(\gamma_{\min}^{KN}) = 1.6 \times 10^4 B_{12}^{-4/3} R_6^{-1} P^{-1} \left( \frac{R_E}{R} \right)^3 (\cos \chi)^{4/3} \text{ s}^{-1} \quad (74)$$

which sharply increases with altitude,  $R_E = R + h_0$ . We approximate the K-N loss rate, modifying Blumenthal & Gould's (1970) formula for scattering of isotropic thermal photons of temperature  $T_6$ , from a hot polar cap of radius  $R_T$ , with a dilution factor that accounts for the fall-off in photon density with height  $h$ :

$$\dot{\gamma}_{\text{KN}}(\gamma_{\min}^{KN}) \simeq \frac{\pi r_0^2}{6mc^2} \frac{(mckT)^2}{\hbar^3} \ln \left( \frac{4\gamma_{\min} kT}{mc^2} \right) \frac{R_T^2}{h^2 + R_T^2} \simeq 7.6 \times 10^8 \text{ s}^{-1} T_6^2 \frac{R_T^2}{h^2} \quad (75)$$

for  $R_T \ll h$  and ignoring the slowly varying  $\ln$  factor. Setting  $\dot{\gamma}_{\text{CR}}(\gamma_{\min}^{KN}) = \dot{\gamma}_{\text{KN}}(\gamma_{\min}^{KN})$  and assuming  $R_E \sim h_0$ ,

$$\left( \frac{h_0}{R} \right)_{KN} \simeq 8.6 B_{12}^{4/15} P^{1/5} R_6^{1/5} T_6^{2/5} \left( \frac{R_T}{R} \right)^{2/5} (\cos \chi)^{-4/15}. \quad (76)$$

Although the above expression involves a number of approximations, it does seem to roughly reproduce our numerical results. For example, taking the parameters  $T_6 = 0.5$ ,  $R_6 = 0.8$ ,  $P = 0.1$ ,  $B_{12} = 4.4$  and  $R_T = 0.04 R$  gives  $h_0/R \simeq 1.6$ , fairly close to the value shown in Fig. 11.

At the altitude  $h_0$ , where CR losses are dominant and curvature photons produce the PFFs, the width of the acceleration zone can be calculated in a similar manner to that of the ICS

controlled acceleration zones. Using the CR critical frequency,  $\varepsilon_{\text{cr}} = (3/2)(\hbar/mc)\gamma^3/\rho_c$  in equation (69), we can solve for the particle energy  $\gamma_{\text{min}}^{CR}$  which produces the minimum acceleration zone width  $S_c$ ,

$$\gamma_{\text{min}}^{CR} = (6C_p A_\gamma^{1/2})^{2/7} = 4.7 \times 10^7 B_{12}^{-1/7} P^{1/7} \left(\frac{R_E}{R}\right)^{4/7} R_6^{1/7} (\cos \chi)^{1/7}, \quad (77)$$

where

$$C_p = \left(\frac{0.2\rho_c}{B'\varepsilon_{\text{cr}}}\right). \quad (78)$$

Then substituting the expression for  $\gamma_{\text{min}}^{CR}$  back into equation (69) for  $S_c$ , we have

$$S_c^{CR} \simeq 4.8 \times 10^4 B_{12}^{-4/7} P^{4/7} R_6^{4/7} \left(\frac{R_E}{R}\right)^{16/7} (\cos \chi)^{-3/7} \text{ cm}. \quad (79)$$

The expression for  $\gamma_{\text{min}}^{CR}$  above is also a very good estimate of  $\gamma_{\text{max}}^{CR}$ , the maximum Lorentz factor of the CR-controlled acceleration zone, because  $S_p \ll S_a$  for CR photons (i.e. the PFF is very close to where the first pairs are produced).

For very high field strengths ( $B' \gtrsim 0.5$ ) both electron and positron ICS operate in the resonant scattering regime. The incident soft photons scatter in the cyclotron resonance and their scattered energies are approximately  $\varepsilon_s \sim \gamma B'$ . In the Thomson limit of resonant scattering, the energy of the scattered photons is independent of incident photon angle. This means that  $S_c^+ = S_c^-$ , PFF<sup>+</sup> will coincide with  $h_0$ , and stable ICS-controlled acceleration zones are thus possible for high-field pulsars. However, in the relatively high fields where resonant ICS controls the positron PFFs, relativistic effects on the resonant scattering cross section as well as photon splitting will become important (as will be discussed in Section 4) and our calculation of PFFs is incomplete.

#### 4. Discussion

In this paper, we have investigated the effect of cascades from downward-accelerated positrons on the electrodynamics of the PC particle acceleration. We find that when ICS produces pairs in the acceleration zone, the positron cascades may screen the accelerating electric field and disrupt particle acceleration near the NS surface. Thus, if lower PFFs can develop, the picture of steady particle acceleration from the PC surface must undergo major revision. We suggest that a stable acceleration zone may exist at an altitude of about one stellar radius above the PC, in which pairs from CR limit the electrostatic acceleration of primaries by screening the electric field near the upper PFF.

The calculations presented here are only a first attempt to describe the physics of what is a very complicated process. We have made many assumptions and approximations to obtain our results. While we believe that the gross qualitative results of our study are correct, there are a number of aspects which should be treated more accurately to achieve more solid quantitative results. We have assumed that the screening of the  $E_{\parallel}$  occurs over the short distance determined

by the upper boundary condition of Poisson’s equation, not by the dynamics of the pair screening. The details of the pair screening also determine the fraction of pairs that return to the PC and we have briefly outlined in Section (2.4) how such a calculation can be done within the electrodynamic framework set up in this paper. A determination of the returning positron fraction would answer some interesting questions, such as whether PC heating is important relative to cooling in setting the PC temperature and if so, whether there is a feedback loop between the formation of the upper PFF and the PC heating. The characteristics of the downward cascades need further study and modeling. While we have done preliminary modeling of these cascades near the PC rim, there will be significant variation in pair yields with magnetic colatitude. Near the magnetic pole, the pair multiplicity will drop, allowing the lower PFF height to decrease or even disappear.

We have found that the nature of the PC acceleration depends strongly on the characteristics of the radiation from the hot PC. Thus, to solidify the quantitative aspects of our results, it is important to treat the thermal PC radiation and the ICS process as accurately as possible. For example, we have assumed in this paper, that the thermal radiation is uniformly emitted over a PC of size  $R_T = 3\theta_0$  with an isotropic flux distribution. However, studies of thermal radiation propagating through a strongly magnetized NS atmosphere (Pavlov et al. 1994) will not be isotropic, due to the anisotropy of the magnetized scattering cross section. The expected radiation pattern consists of a pencil component, beamed along the magnetic field and a fan component perpendicular to the field. Such a beam pattern has been found to be consistent with observed thermal X-rays pulse fractions and pulse profiles for several pulsars (Shibanov et al. 1995, HM98). In addition, our treatment of ICS uses a combination of the (non-relativistic) magnetized cross section in the Thomson limit for scattering near the fundamental cyclotron resonance, and the (non-magnetic) Klein-Nishina cross section to describe relativistic effects above the resonance. While this hybrid treatment is somewhat inaccurate for  $B \gtrsim 0.1 B_{\text{cr}}$  and therefore not completely satisfactory, the fully relativistic QED magnetic scattering cross section (e.g. DH86) is too complicated for use in this type of calculation. In particular, the quantization of the electron momentum perpendicular to the field limits the number of Landau states contributing to the cross section for each incident photon energy. The magnetic QED cross section for scattering just above the fundamental cyclotron resonance, and therefore the loss rate, could therefore be substantially lower than the Klein-Nishina cross section we have used here. Unfortunately, there exists no simplified, approximate expression for the QED scattering cross section, which smoothly bridges, and allows a unified treatment of, the relativistic resonant and non-resonant regimes of ICS.

A physical process which we have neglected in this study, photon splitting, is not expected to be significant for the magnetic fields we have considered, but will be very important for pulsars having surface  $B_0 \gtrsim 0.5 B_{\text{cr}}$ . Photon splitting, a third-order QED process in which one photon splits into two, operates only in very high magnetic fields and competes as an attenuation process with one-photon pair production (Harding et al. 1997) because it can occur below pair threshold. The implications of photon splitting for PC PFFs is profound. Pulsars having  $B_0 \gtrsim 0.5 B_{\text{cr}}$  will produce fewer pairs, especially near the surface, so that the cascades from downward-moving

positrons may not produce a lower PFF. This is about the same field strength where we found that double PFFs controlled by resonant ICS at the NS surface become possible. Thus, the stable, CR-controlled double PFF structure we have studied in this paper, which we found to move to higher altitudes with increasing surface field strength, will eventually collapse back to the surface at very high  $B_0$ . A single PFF will then form, controlled by ICS, and the acceleration zone will have characteristics similar to that shown in Figure 6. At extremely high surface fields,  $B_0 \gtrsim 1.0 B_{\text{cr}}$  photon splitting will suppress pair creation completely at this single PFF, and the pulsar may be radio quiet (Baring & Harding 1998). However, the particle acceleration in these pulsars will operate very efficiently, free of any screening of  $E_{\parallel}$ , so they are expected to be observable at high energies. Bound-state pair production, where photons convert to positronium just below pair threshold rather than converting to free pairs (Usov & Melrose 1995), may also come into play at higher field strengths.

Some of the main results that we have presented in this paper have some important implications for pulsar high-energy emission. One of these results is the insensitivity of the acceleration voltage (maximum particle energy)  $\gamma_{\text{max}}$  to any pulsar parameters such as period, surface magnetic field strength, obliquity (except for nearly orthogonal rotators), and even height. This result showed up many times in the course of our calculations (cf. Figs. 4, 5, 6, 11 and 12, and equation [77]), and seems to be a robust characteristic of this type of PC acceleration model. The maximum particle acceleration energy varies only within each pulsar, as a function of magnetic colatitude. This energy, between  $5 \times 10^{12}$  eV and  $5 \times 10^{13}$  eV for CR-controlled acceleration zones, is about two to three times higher than that without frame-dragging (e.g. A83), and is consistent with the primary particle energy required in CR-initiated PC cascade models of  $\gamma$ -ray pulsars (e.g. DH96). The acceleration energy is very high near the magnetic poles, where the radius of curvature goes to infinity, allowing for the possibility of a narrowly beamed, hard component in  $\gamma$ -ray pulses. However, the radiation power emitted by these high-energy particles will be small, because the curvature radiation loss rate is proportional to  $\rho_c^{-2}$ . The insensitivity of  $\gamma_{\text{max}}$  to pulsar parameters implies that the primary particles in all pulsars are accelerated to the same energy, and that the luminosity of the high-energy emission should depend only of the flux of primary particles. This is consistent with trends in the observed  $\gamma$ -ray pulsar luminosities (Thompson et al. 1997). The  $\gamma$ -rays will originate within a stellar radius of the upper stable PFF, at height  $h_c = h_0 + S_c^-$ . From our results of Figs. 10 and 11, and equations (76) and (79), the height of the  $\gamma$ -ray production increases with period, roughly as  $P^{1/2}$ . The standard PC half-angle at height  $R_{\gamma} = R + h_c$  will be  $\theta_c \simeq (\Omega R_{\gamma}/c)^{1/2} \propto P^{-1/4}$ . Thus, the  $\gamma$ -ray emission solid angle  $\Omega_{\gamma}$ , which is expected to be,  $\Omega_{\gamma} \simeq 2\pi[1 - \cos(3\theta_c/2)]$ , will be very weakly dependent on period and field strength.

Our conclusion that stable acceleration may occur in most pulsars at some altitude above the surface will have consequences not only for high-energy emission, but for radio emission as well. If electron-positron pairs are necessary for coherent radio emission, then the dependence of the PFF altitude on pulsar parameters should be taken into account when determining the radio pulsar

“death line”, the line on the period-period derivative diagram beyond which pulsars are incapable of producing pairs. Our calculations in this paper suggest that pulsars with long periods do not produce PFFs, and that there will be a “death line” at periods below where there are observed radio pulsars. But this is a long-standing problem of PC acceleration, most recently discussed by Arons (1998), and one that should be addressed in future studies.

Our principal findings can be summarized as follows.

1. Lower PFFs may form by positrons returning to the NS surface from the upper PFF.
2. Pair creation by the ICS process dominates near the stellar surface, but is not symmetric for upward and downward going particles, so that stable, double PFF formation is very unlikely.
3. Stable, self-consistent double PFFs can only exist when they are formed by CR. They can only form at a height above the surface where CR becomes dominant.
4. The maximum particle energy is insensitive to any pulsar parameters such as period, surface magnetic field strength, obliquity, even height, and is sufficient to power  $\gamma$ -ray pulsars.

The main conclusion of this paper is that the cascades from positrons returning to the PC may have a significant effect on the primary particle acceleration in pulsars and should not be neglected. It is possible that lower PFFs do not form for all pulsars, and may not form over the entire PC. A detailed study of the screening of the accelerating electric field by the returning positron cascades is beyond the scope of this paper, but will ultimately be necessary to understand PC acceleration. These studies are needed to address the questions of the returning positron fraction and the multiplicity of downward cascades. If we can show that the returning positrons do not screen  $E_{\parallel}$ , then the present assumption of acceleration right from the NS surface is valid. But if these studies show that screening at a lower PFF is effective, then the possibility of acceleration above the NS surface must be incorporated in PC models.

We thank the referee Bing Zhang for his very careful review and insightful comments. We are also grateful to Joe Daugherty, for help in the downward cascade simulations, to Steve Sturmer for discussions on inverse-Compton scattering and Matthew Baring for comments on the manuscript.

## APPENDIX A. APPROXIMATE EXPRESSIONS FOR THE ACCELERATING ELECTRIC FIELD

Here we present the explicit expressions for the electric field component parallel to the magnetic field for the various ranges of altitude. These expressions have not been rescaled to allow for acceleration starting at an effective radius above the stellar surface, so that  $z$  is the altitude above the surface.

$\mathbf{S}_c \ll \mathbf{r}_{\text{pc}}$ , and  $0.1 \mathbf{r}_{\text{pc}}(\mathbf{r}_{\text{pc}}/\mathbf{R}) \ll \mathbf{s} \leq \mathbf{S}_c$ :

$$E_{\parallel} \simeq -3 \frac{\Omega R}{c} \frac{B_0}{1-\epsilon} \left(1 - \frac{z}{z_c}\right) z z_c \left[ \kappa \cos \chi + \frac{1}{2} \Theta_0 \xi H(1) \delta(1) \sin \chi \cos \phi \right], \quad (\text{A1})$$

$\mathbf{S}_c \ll \mathbf{r}_{\text{pc}}(\mathbf{r}_{\text{pc}}/\mathbf{R})$ , and  $\mathbf{s} \ll \mathbf{S}_c$ :

$$E_{\parallel} \simeq -\frac{3}{2} \left(\frac{\Omega R}{c}\right)^2 \frac{B_0}{f(1)} (1-\xi^2) z \left[ \kappa \cos \chi + \frac{1}{4} \Theta_0 \xi H(1) \delta(1) \sin \chi \cos \phi \right], \quad (\text{A2})$$

$\mathbf{S}_c < \mathbf{r}_{\text{pc}}/3$ , and  $\mathbf{s} \leq \mathbf{S}_c$ :

$$E_{\parallel} \simeq -3 \frac{\Omega R}{c} \frac{B_0}{1-\epsilon} \left(1 - \frac{z}{z_c}\right) z \left[ \kappa \cos \chi + \frac{1}{2} \Theta_0 \xi H(1) \delta(1) \sin \chi \cos \phi \right], \quad (\text{A3})$$

$\mathbf{s} \gtrsim \mathbf{r}_{\text{pc}}/3$  and  $\mathbf{s} \leq \mathbf{S}_c$ :

$$\begin{aligned} E_{\parallel} \simeq & -\frac{3}{2} \left(\frac{\Omega R}{c}\right)^2 \frac{B_0}{f(1)} \left\{ \kappa \frac{1}{\eta^4} \left[ (1-\xi^2) - \left(\frac{\eta}{\eta_c}\right)^3 \sum_{i=1}^{\infty} \frac{8J_0(k_i \xi)}{k_i^3 J_1(k_i)} e^{-\gamma_i(\eta_c)(\eta_c-\eta)} \right] \cos \chi \right. \\ & + \frac{1}{4} \Theta_0 \left[ \frac{f(1)}{f(\eta)} \right]^{1/2} F(\eta) \frac{1}{\eta^{1/2}} \left[ \xi(1-\xi^2) - \frac{\eta_c F(\eta_c)}{\eta F(\eta)} \right. \\ & \left. \left. \sum_{i=1}^{\infty} \frac{16J_1(\tilde{k}_i \xi)}{\tilde{k}_i^3 J_2(\tilde{k}_i)} e^{-\tilde{\gamma}_i(\eta_c)(\eta_c-\eta)} \right] \sin \chi \cos \phi \right\}, \end{aligned} \quad (\text{A4})$$

which translates into

$$E_{\parallel} \simeq -\frac{3}{2} \left(\frac{\Omega R}{c}\right)^2 \frac{B_0}{f(1)} (1-\xi^2) \left[ \kappa \cos \chi + \frac{1}{4} \Theta_0 \xi H(1) \delta(1) \sin \chi \cos \phi \right], \quad (\text{A5})$$

when  $\mathbf{s} \ll \mathbf{S}_c$ .

Here

$$\begin{aligned} F(\eta) = & -\frac{2}{\eta} \left( \epsilon - \frac{2\kappa}{\eta^2} \right) + \frac{3}{(1-\epsilon/\eta)f} \left[ \frac{1}{\eta} \left( \epsilon - \frac{\kappa}{\eta^2} \right) \right. \\ & \left. - \frac{1}{(1-\epsilon/\eta)} \left( \frac{4}{3} - \frac{\epsilon}{\eta} - \frac{3}{2f} \right) \left( 1 - \frac{3\epsilon}{2\eta} + \frac{\kappa}{2\eta^3} \right) \right], \end{aligned}$$

$$\Theta_0 = \left[ \frac{\Omega R}{c} \frac{1}{f(1)} \right]^{1/2}.$$

In the above expressions  $r_{pc} \approx \Theta_0 R$  is the PC radius,  $z_c \equiv S_c/R$  is the dimensionless altitude of the upper boundary (PFF), and all other quantities are scaled with the true stellar radius. Note also that  $H(1)\delta(1) \approx 1$ .



## REFERENCES

- Arons, J. 1981, in IAU Symp. 95, Pulsars, ed. W. Sieber & Wielebinski (Dordrecht: Reidel), 69
- Arons, J. 1983, ApJ, 266, 215: A83
- Arons, J. 1998, in Neutron Stars and Pulsars, eds. N. Shibazaki, N. Kawai, S. Shibata & T. Kifune (University Academy Press: Tokyo), p. 339.
- Arons, J., & Scharlemann, E. T. 1979, ApJ, 231, 854: AS79
- Baring, M. G. & Harding, A. K. 1998, in preparation.
- Becker, W., & Trümper, J. 1997, A&A, 326, 682
- Bussard, R. W., Alexander, S. B., & Meszaros, P. 1986, *Phys. Rev. D*, 34, 440
- Canuto, V., Lodenguai, J., & Ruderman, M. 1971, *Phys. Rev. D*, 3, 2303
- Daugherty, J. K., & Harding, A. K. 1983, ApJ, 273, 761: DH83
- Daugherty, J. K., & Harding, A. K. 1986, ApJ, 309, 362: DH86
- Daugherty, J. K., & Harding, A. K. 1989, ApJ, 336, 861.
- Daugherty, J. K., & Harding, A. K. 1996, ApJ, 458, 278: DH96
- Dermer, C. 1990, ApJ, 360, 197: D90
- Deutsch, A. 1955, Ann. d’Ap., 18, 1
- Fawley, W. M., Arons, J., & Scharlemann, E. T. 1977, ApJ, 164, 529
- Goldreich, P., & Julian, W. H., 1969, ApJ, 157, 869
- Gonthier, P. L. & Harding, A. K., 1994, ApJ, 425, 767
- Harding, A. K., Baring, M. G. & Gonthier, P. G. 1997, ApJ, 476, 246.
- Harding, A. K., & Muslimov, A. G. 1998, in Neutron Stars and Pulsars, eds. N. Shibazaki, N. Kawai, S. Shibata & T. Kifune (University Academy Press: Tokyo), p. 311. (astro-ph/9802038)
- Harding, A. K., & Muslimov, A. G. 1998, ApJ, in press. (astro-ph/9802044)
- Jones, P. B. 1978, MNRAS, 184, 807
- Jones, P. B. 1985, Phys. Rev. Lett., 55, 1338
- Jones, P. B. 1986, MNRAS, 218, 477

- Kardashëv, N. S., Mitrofanov, I. G., & Novikov, I. D. 1984, *Sov. Astron.*, 28, 651
- Lorentz, C. P., Ravenhall, D. G., & Pethick, C. J. 1993, *Phys. Rev. Lett.*, 70, 379
- Mestel, L. 1998, *Stellar Magnetism* (Oxford: Oxford University Press)
- Muslimov, A. G., & Harding, A. K. 1997, *ApJ*, 485, 735: MH97
- Muslimov, A. G., & Tsygan, A. I. 1990, *AZh*, 67, 263: MT90
- Muslimov, A. G., & Tsygan, A. I. 1992, *MNRAS*, 255, 61: MT92
- Neuhauser, D., Langanke, K., & Koonin, S. E. 1986, *Phys. Rev.*, A33, 2084
- Neuhauser, D., Koonin, S. E., & Langanke, K. 1987, *Phys. Rev.*, A36, 4163.
- Pavlov, G. G., Shibanov, Yu A., Ventura, J. & Zavlin, V. E. 1974, *A & A*, 289, 837.
- Ravenhall, D. G., & Pethick, C. J. 1994, *ApJ*, 424, 846
- Ruderman, M. A., & Sutherland, P. G. 1975, *ApJ*, 196, 51: RS75
- Shibanov, Yu. A., Zavlin, V. E., Pavlov, G. G. & Ventura, J. 1995, in 17th Texas Symposium on relativistic Astrophysics, eds. H. Bohringer, G. Morfill & J. Trumper, *Annals of NY Acad. Sci.*, 759, p. 291.
- Sturner, S. J. 1995, *ApJ*, 446, 292: S95
- Sturner, S. J. & Dermer, C. D. 1994, *ApJ*, 420, L79.
- Sturrock, P. A. 1971, *ApJ*, 164, 529
- Thompson, D. J., Harding, A.K., Hersen, W. & Ulmer, M.P. 1997, in *Proc. of the 4th Compton Symposium*, ed. C.D. Dermer, M.S. Strickman & J.D. Kurfess (AIP 410: New York), 39.
- Tsai, W.-Y. & Erber, T. 1974, *Phys. Rev. D*, 10, 492.
- Usov, V.V. & Melrose, D. B. 1995, *Aust. J. Phys.*, 48, 571.
- Wang, F. Y.-H., Ruderman, M., Halpern, J. P., & Zhu, T. 1998, *ApJ*, in press
- Xia, X. Y. et al. 1985, *A&A*, 152, 93.
- Zavlin, S.E., Shibanov, Yu. A. & Pavlov, G.G. 1995, *Astron. Lett.*, 21, 149.
- Zhang, B., & Qiao, G. J. 1996, *A&A*, 310, 135
- Zhang, B., Qiao, G. J., Liu, W. P., & Han, J. L. 1997, *ApJ*, 478, 313: ZQLH97

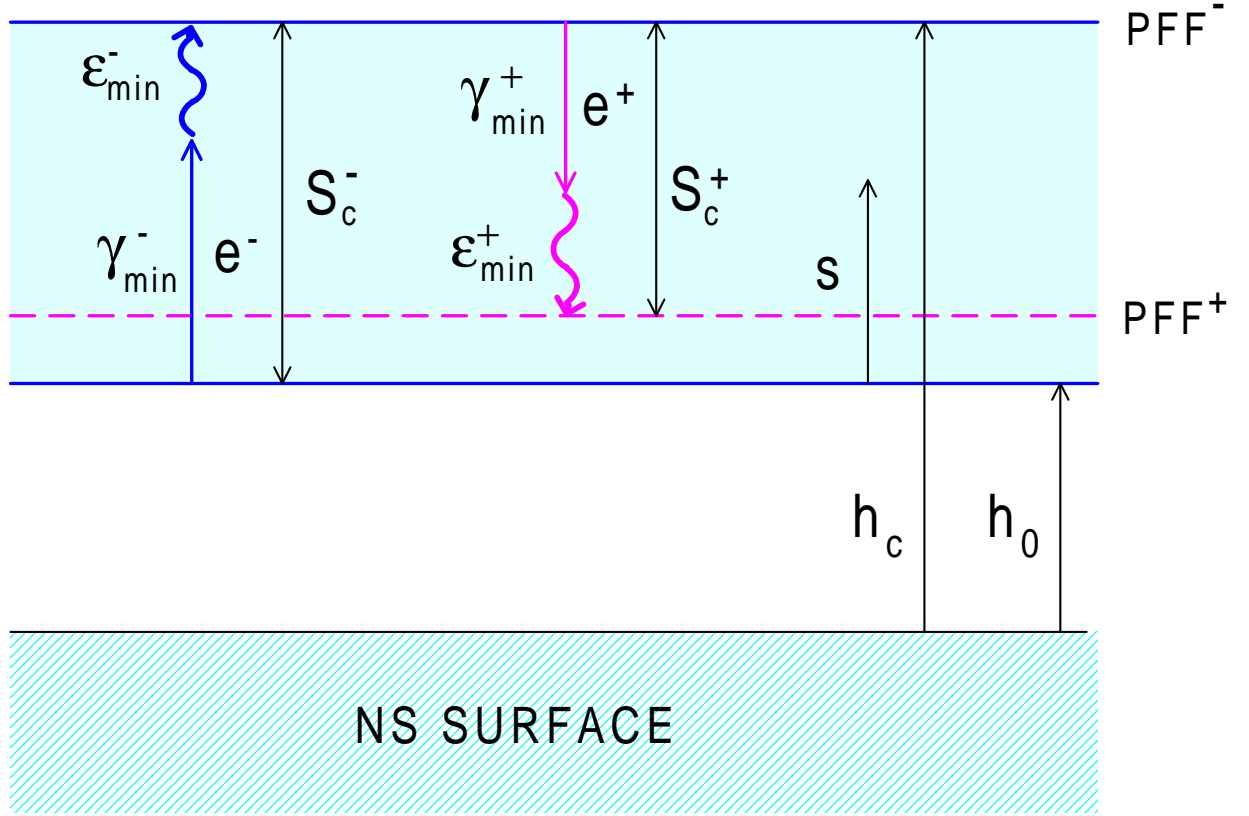


Fig. 1.— Schematic illustration of the double pair formation fronts (PFF) produced by electrons and positrons at height  $h_0$  above a pulsar PC. Parallel electric field accelerates particles in the shaded zone, up to the electron PFF<sup>-</sup> at height  $h_c$ , and is screened ( $\mathbf{E} \cdot \mathbf{B} = 0$ ) everywhere else. Upward accelerating electrons of energy  $\gamma_{\min}^-$  radiate photons of energy  $\epsilon_{\min}^-$  that can produce the first electron-positron pairs to form the PFF<sup>-</sup>. Downward accelerating positrons of energy  $\gamma_{\min}^+$  radiate photons of energy  $\epsilon_{\min}^+$  that produce pairs which may screen the electric field at PFF<sup>+</sup>. This configuration shows double ICS-controlled PFFs, which are not stable because the positron PFF<sup>+</sup> lies about  $h_0$ .

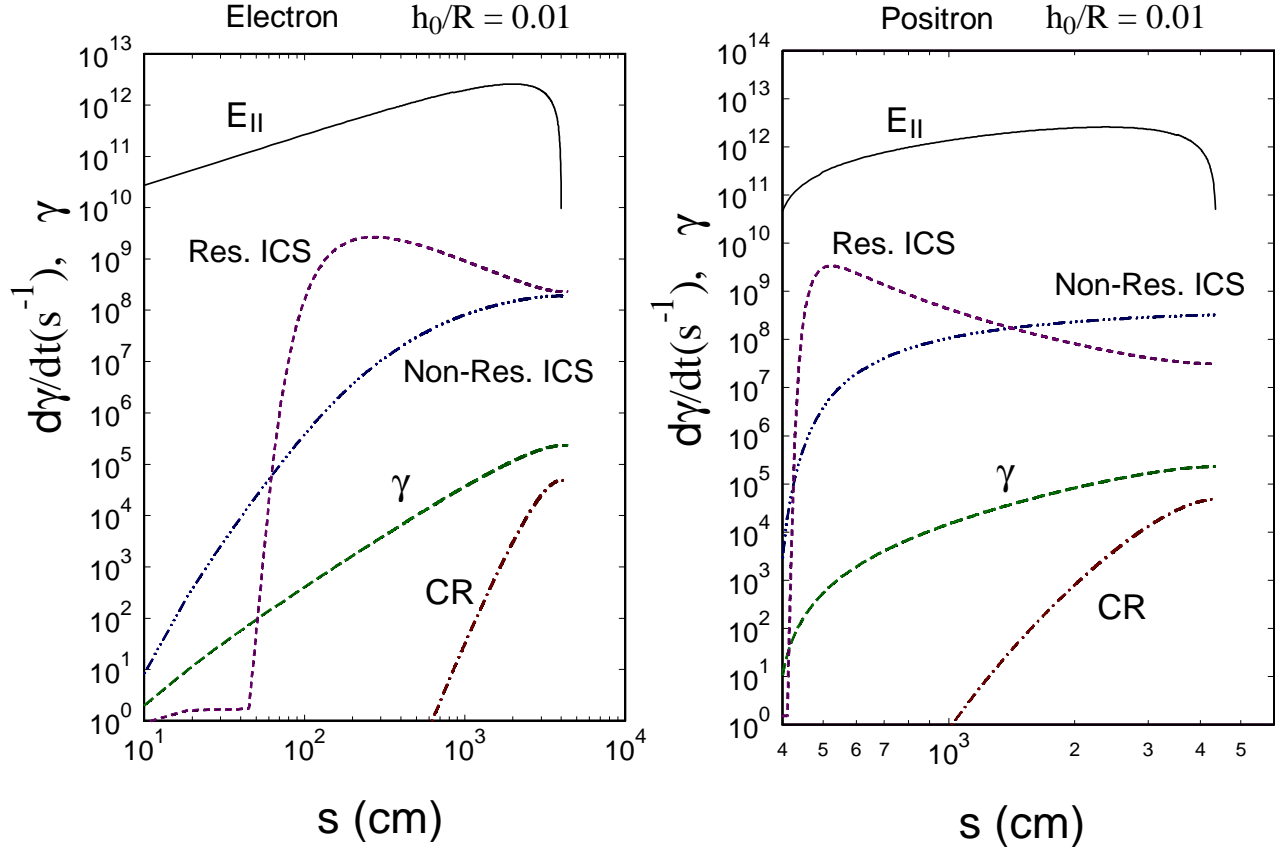


Fig. 2.— Parallel electric field  $E_{\parallel}$ , particle energy  $\gamma$  and energy loss rates  $\dot{\gamma}$  due to non-resonant and resonant ICS and CR as a function of acceleration length  $s$  for ICS-controlled PFFs of electrons (left panel) and positrons (right panel). Here,  $h_0$  is the height of the lower PFF (start of acceleration) above the surface,  $T_6 = 0.5$ ,  $P = 0.1$  s,  $B = 0.1 B_{\text{cr}}$ ,  $\chi = 0.2$  (radians), and  $\xi = 0.7$ .

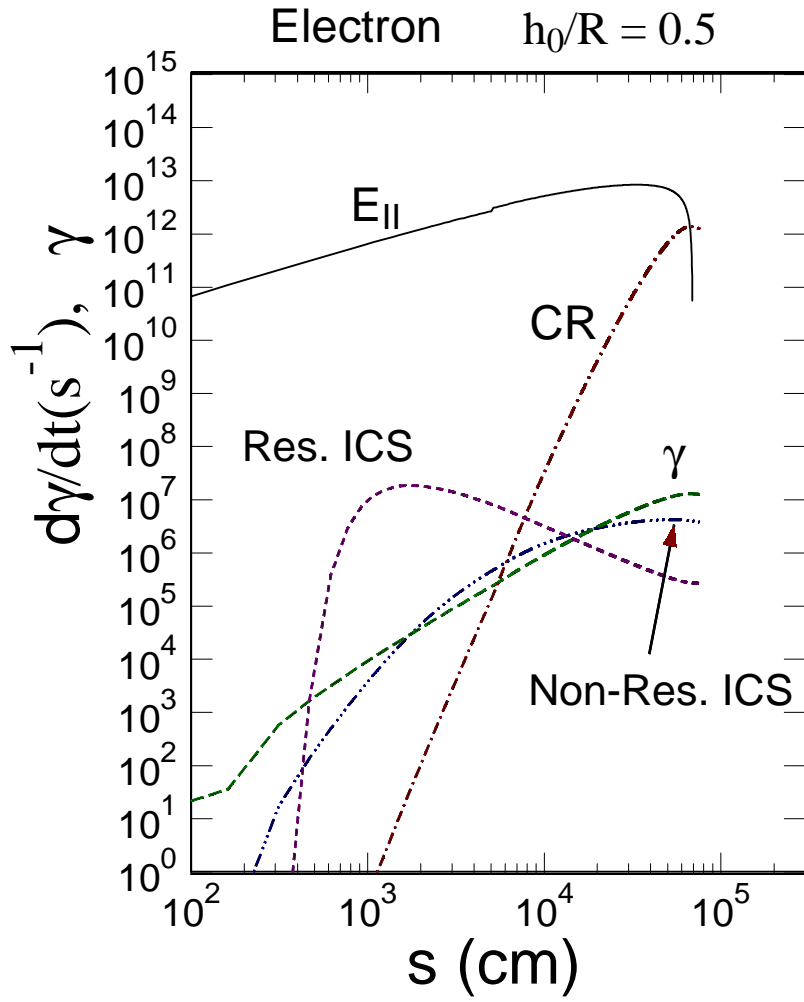


Fig. 3.— Same as Fig. 2, but for the electron CR-controlled PFF at height  $h_0 = 0.5R$ .

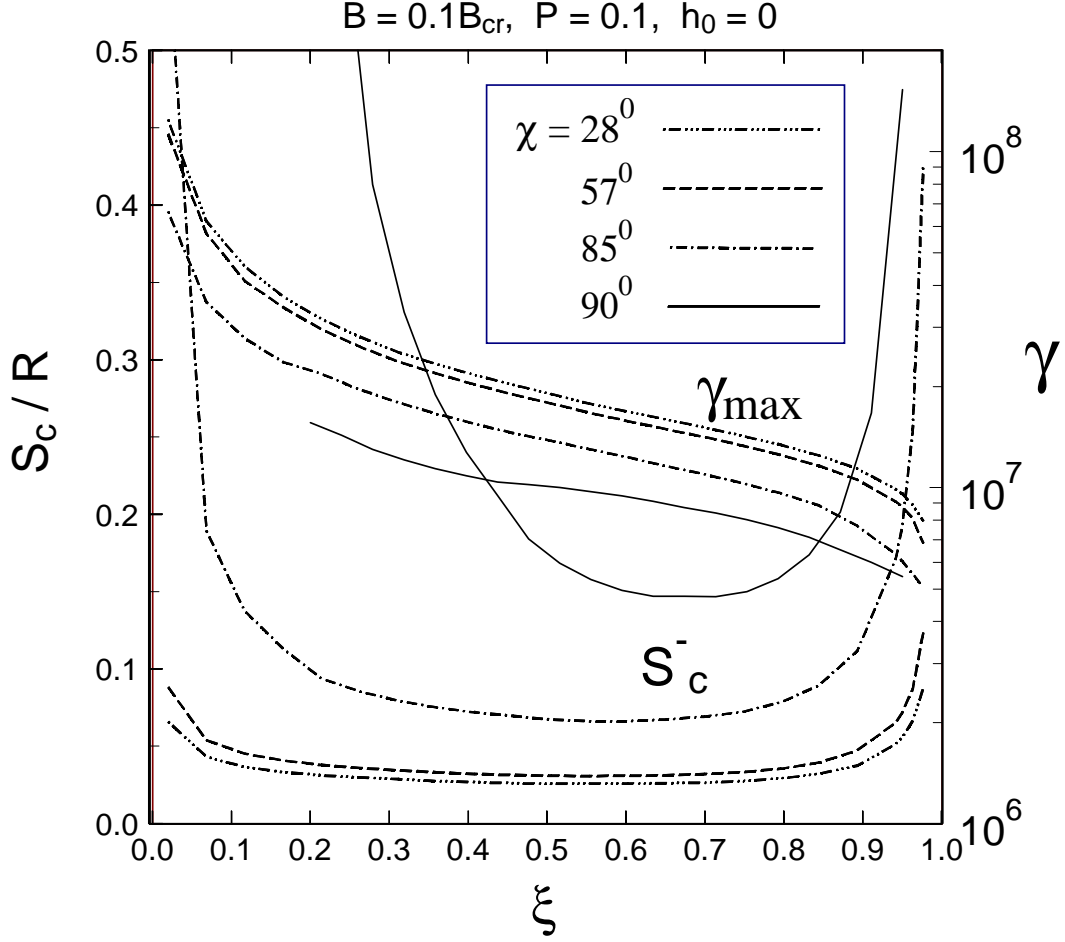


Fig. 4.— Profiles of the acceleration voltage (maximum electron Lorentz factor)  $\gamma_{\text{max}}$  and width,  $S_c^-$ , of the acceleration zone formed by a CR-controlled PFF at the NS surface, neglecting losses and pairs from ICS, as a function of magnetic colatitude scaled to the PC half angle  $\xi = \theta/\theta_0$ , for different obliquities  $\chi$ .

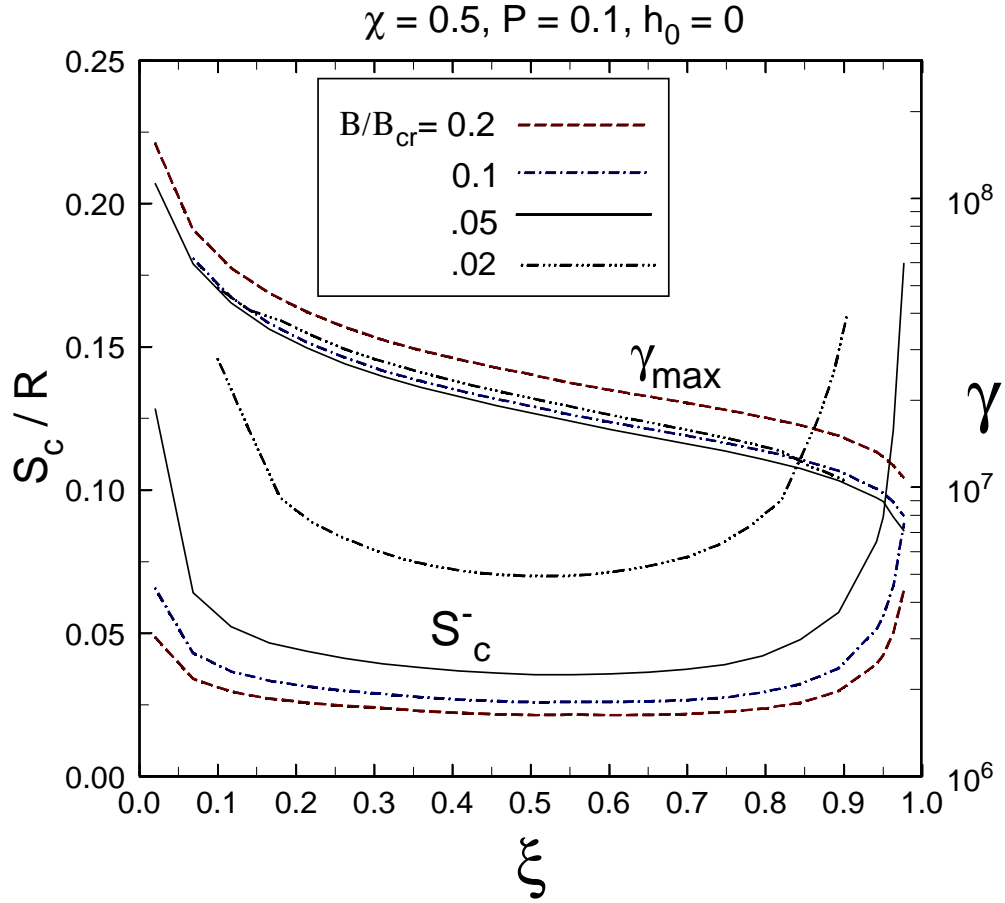


Fig. 5.— Same as Fig. 4 but for different values of the surface magnetic field strength. In Figs. 5-10,  $\chi$  is in radians.

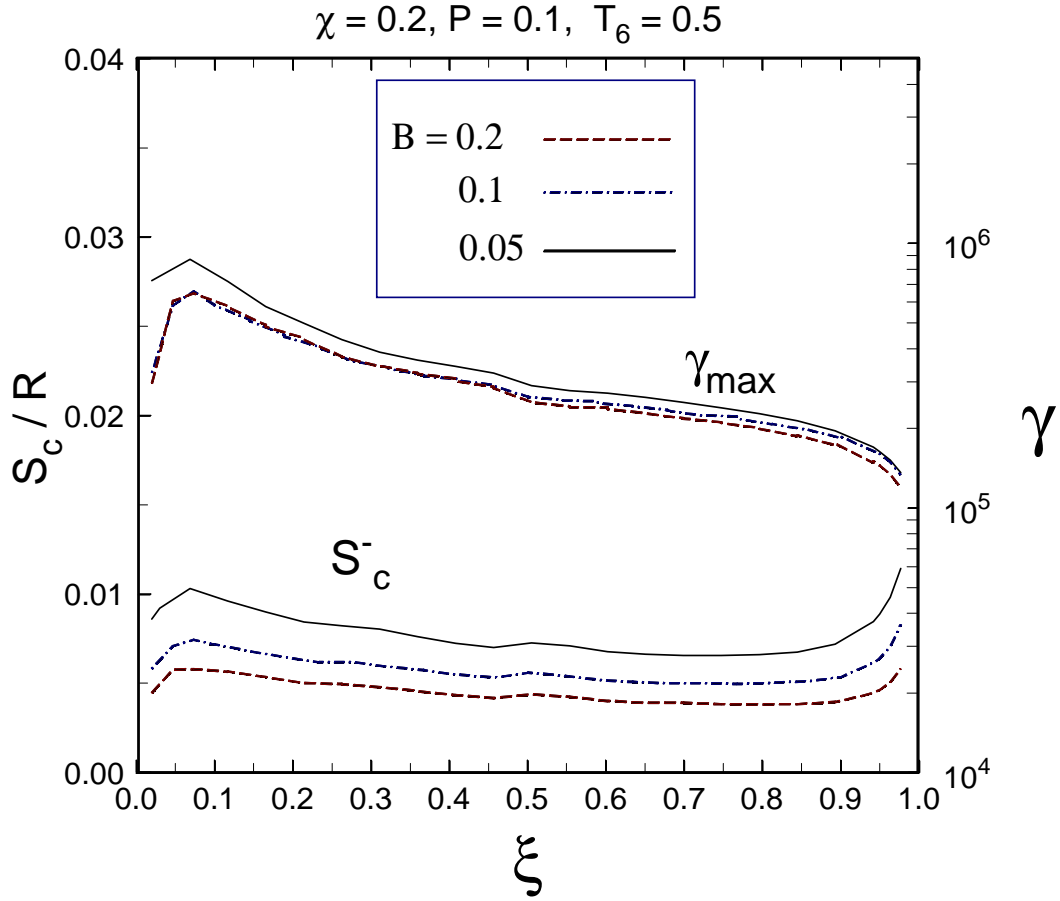


Fig. 6.— Same as Fig. 5 but for ICS-controlled PFFs at the NS surface.



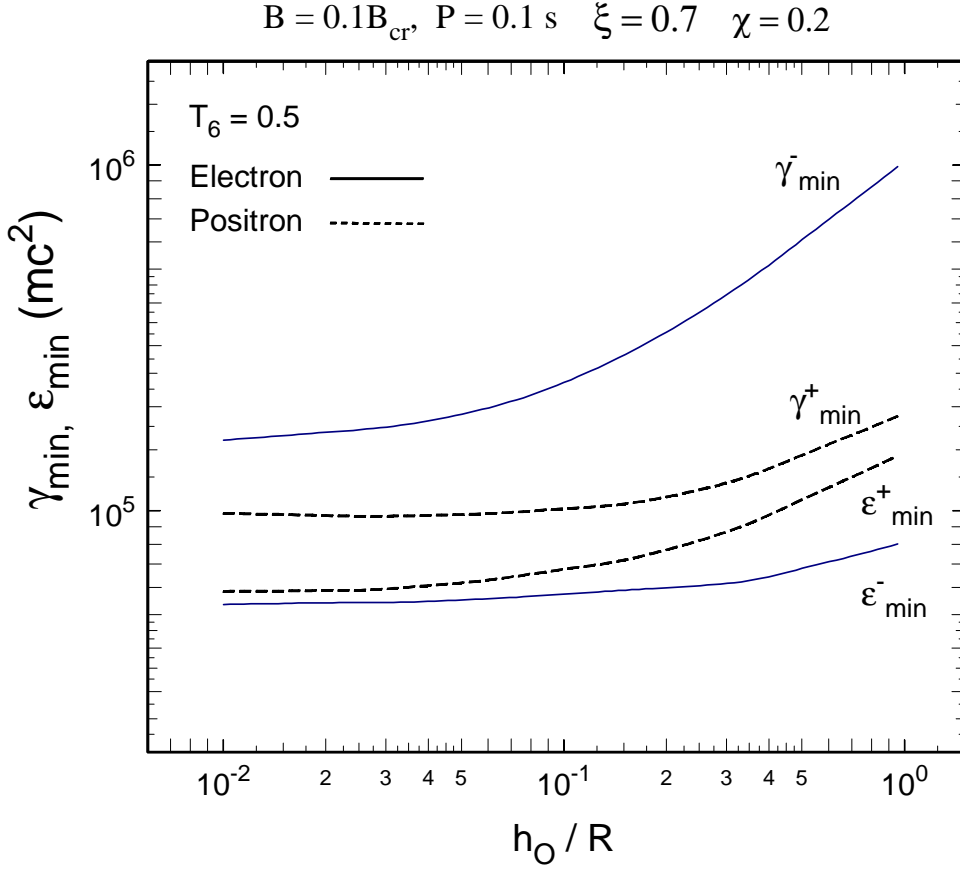


Fig. 7.— Minimum Lorentz factors of electrons,  $\gamma_{\text{min}}^-$ , and positrons,  $\gamma_{\text{min}}^+$  that radiate pair-producing ICS photons of energy  $\epsilon_{\text{min}}^-$  and  $\epsilon_{\text{min}}^+$ , as a function of acceleration starting height  $h_0$ .

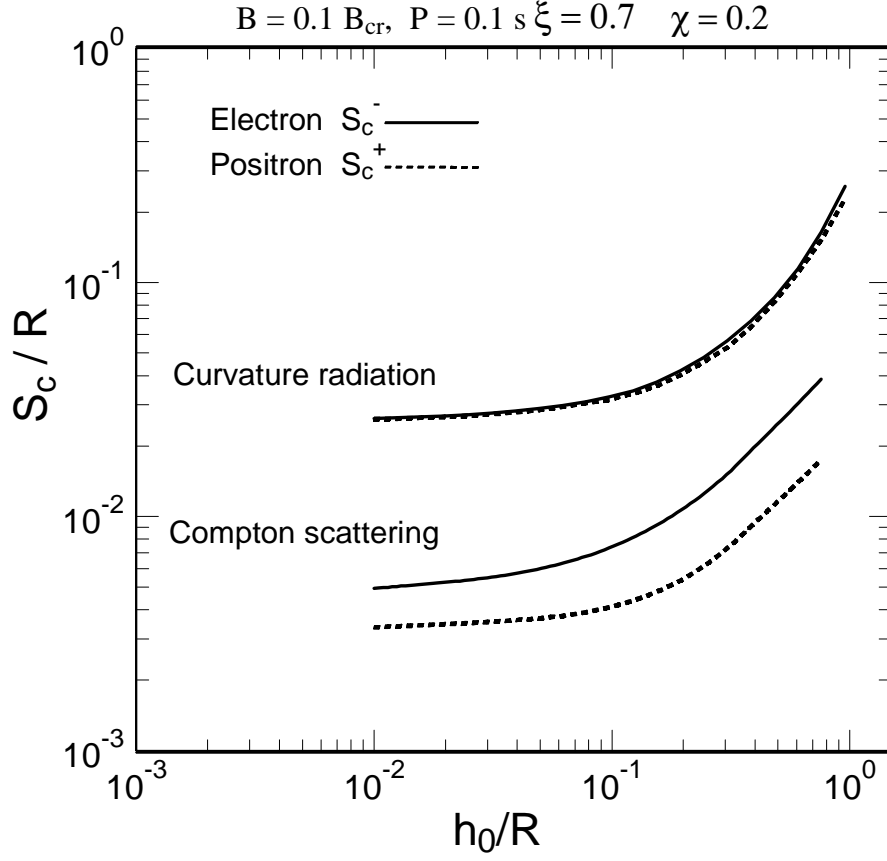


Fig. 8.— Total positron ( $S_c^+$ ) and electron ( $S_c^-$ ) acceleration lengths for CR-controlled and ICS-controlled PFFs as a function of acceleration starting height  $h_0$ .

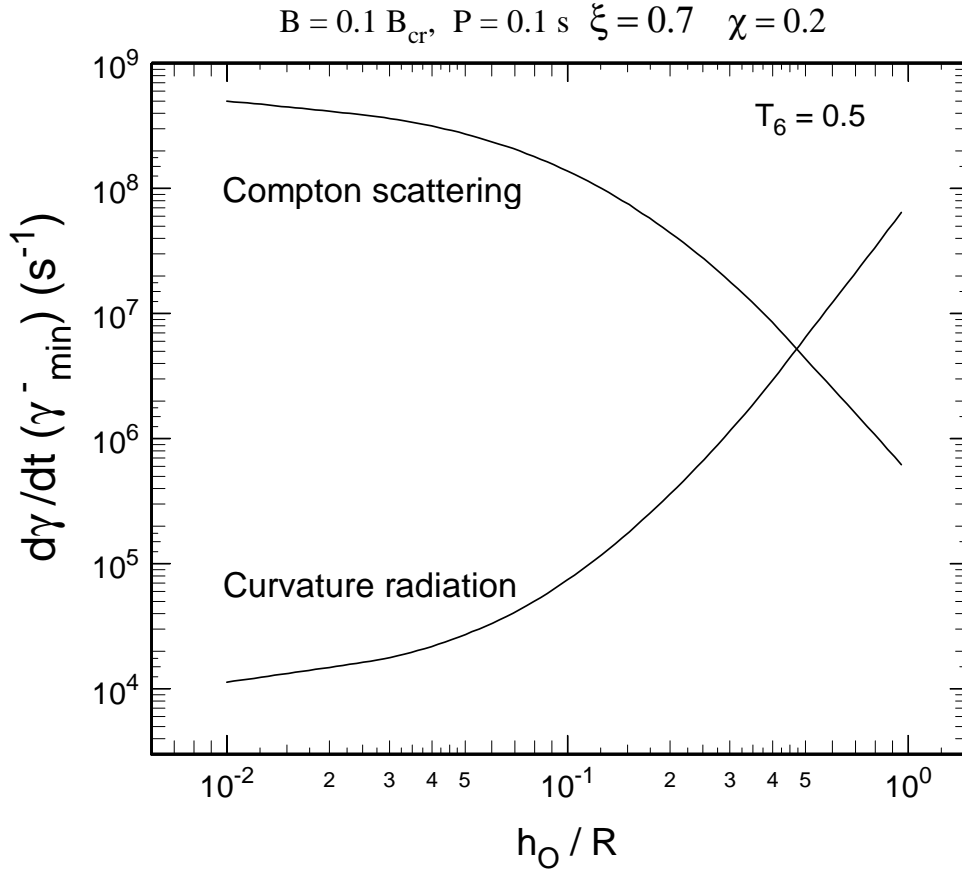


Fig. 9.— Electron energy loss rates for CR and ICS at Lorentz factors  $\gamma_{\text{min}}^-$ , as a function of acceleration starting height  $h_0$ .

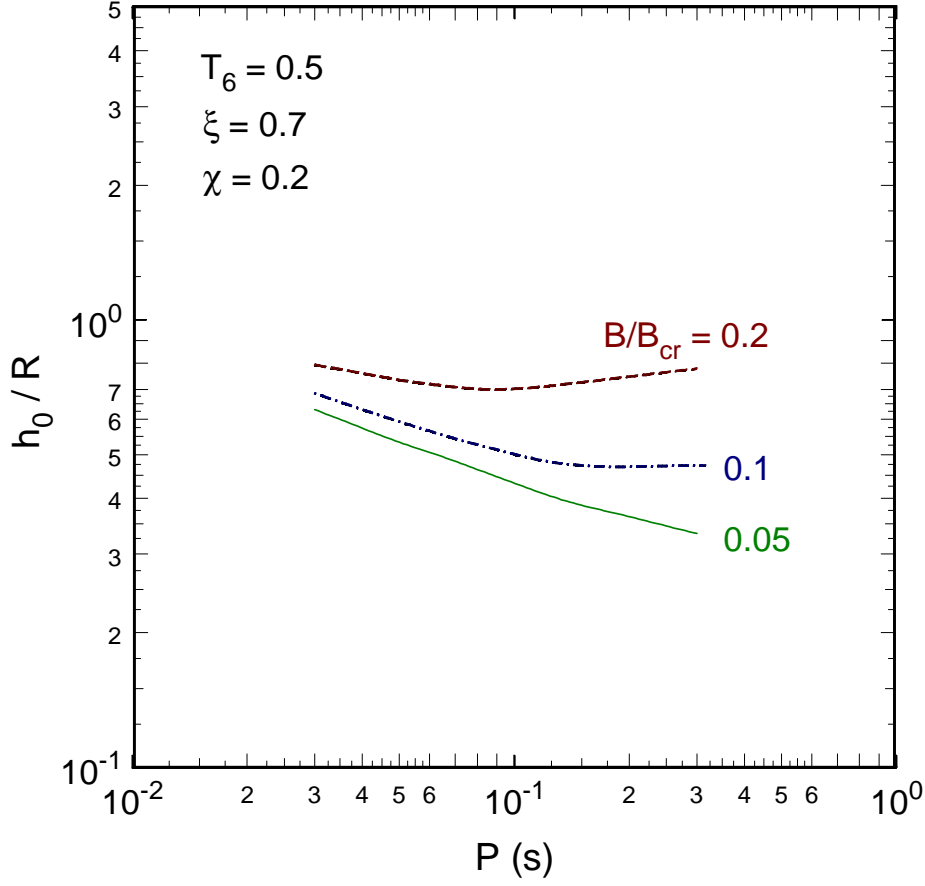


Fig. 10.— Height at which electron energy losses, at Lorentz factors  $\gamma_{\min}^-$ , from CR and ICS are equal, above which the electron PFF is controlled by CR, as a function of pulsar period and surface value of magnetic field strength.

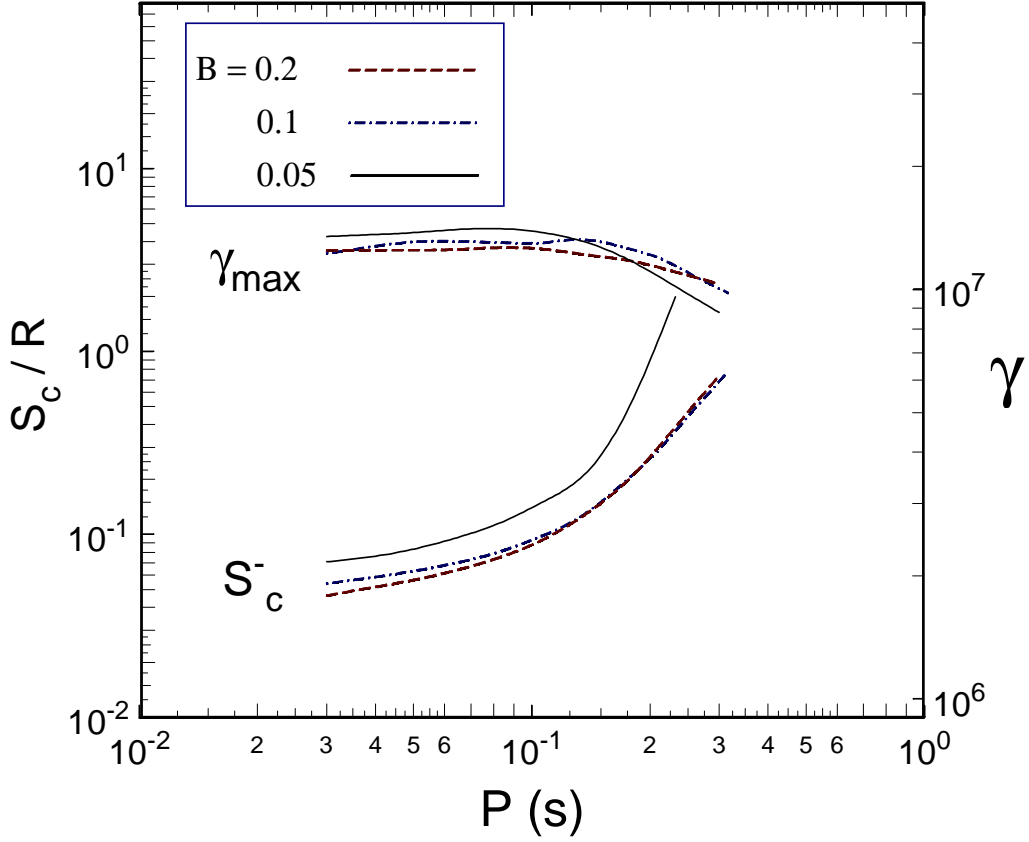


Fig. 11.— Acceleration voltage (maximum electron Lorentz factor)  $\gamma_{\max}$  and width,  $S_c^-$ , of the acceleration zone formed by a CR-controlled electron PFF at the height  $h_0$  where control of the electron PFF switches from ICS to CR (see Fig. 10), as a function of pulsar period and surface value of magnetic field strength.

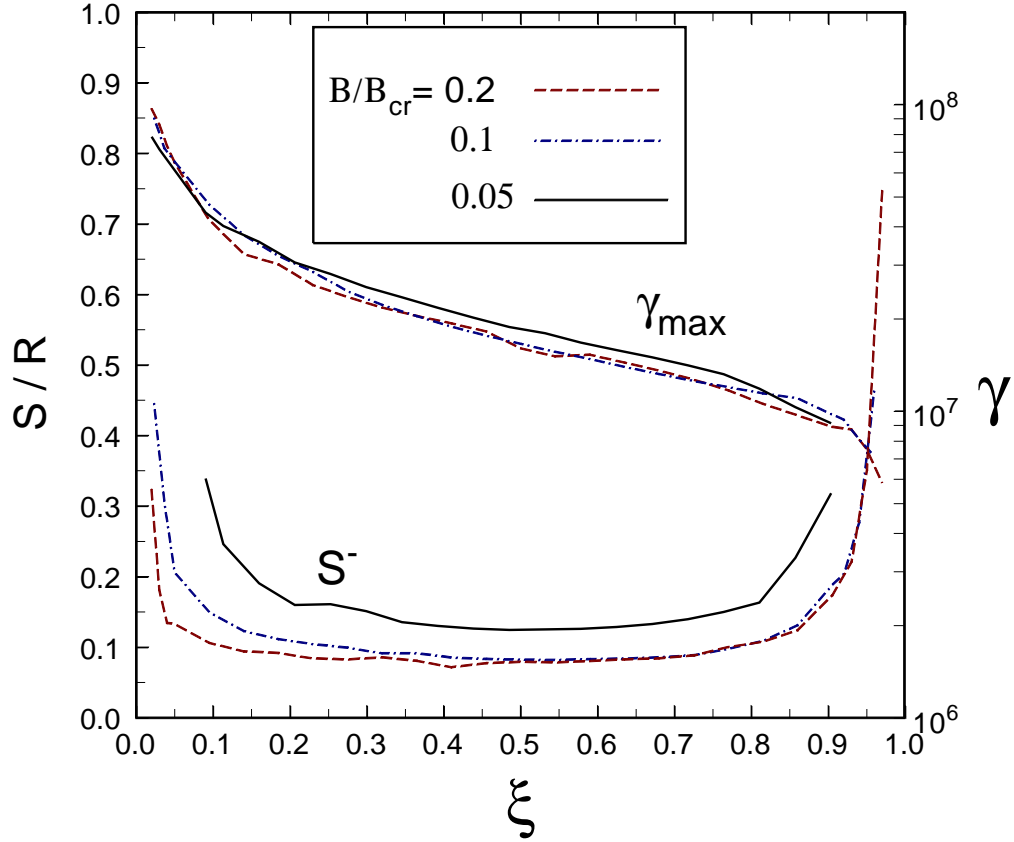


Fig. 12.— Profiles of the acceleration voltage (maximum electron Lorentz factor)  $\gamma_{max}$  and width,  $S_c^-$ , of the acceleration zone formed by a CR-controlled PFF at the height  $h_0$  where control of the electron PFF switches from ICS to CR (see Fig. 10), as a function of magnetic colatitude scaled to the polar cap half angle  $\xi = \theta/\theta_0$ , for different values of surface magnetic field strength.